Geophysical Journal International

Geophys. J. Int. (2025) **242,** 1–20
Advance Access publication 2025 May 19
GJI Seismology

https://doi.org/10.1093/gji/ggaf165

Impact of connected secondary fractures on the seismic reflectivity of large primary fractures

Edith Sotelo [1,*] J. Germán Rubino [2] Nicolás D. Barbosa [1,†] Santiago G. Solazzi[1,‡] and Klaus Holliger[1]

[1] *Institute of Earth Sciences, University of Lausanne, CH-1015 Lausanne, Switzerland. E-mail: edith.sotelo@mines.edu*
[2] *CONICET, Centro Atómico Bariloche—CNEA, San Carlos de Bariloche, 8400 Río Negro, Argentina*

Accepted 2025 April 30. Received 2025 March 24; in original form 2024 November 4

SUMMARY

Large fractures tend to dominate the hydraulic and mechanical properties of fracture networks and, consequently, of fractured rock masses. Hence, their characterization is of primary interest in a variety of applications. Seismic reflection is a non-invasive tool that allows for the characterization of large fractures due to the high mechanical contrast that they commonly present with respect to their embedding background. Smaller secondary fractures are generally connected to the large primary fractures, thus, creating a network for fluid flow. This, in turn, allows for wave-induced fluid pressure diffusion (FPD) to prevail between the intersecting secondary and the large primary fractures, which may have a pronounced, albeit as of yet unexplored, impact on the compliance and the reflectivity of the large primary fractures. To explore this fundamental problem, we investigate the impact that such FPD process has on the compliance and the reflectivity of large primary fractures. To this end, we consider several canonical models, which comprise an infinite horizontal primary fracture connected to vertical smaller secondary fractures embedded in a background deemed impermeable throughout the seismic frequency range. The individual models differ only with regard to the secondary fracture properties (e.g. length, aperture, mechanical moduli). For comparison, we also consider a reference model that disregards the secondary fractures. To constrain the effect of FPD on the primary fracture, we evaluate its effective seismic response by means of vertical compressional oscillatory tests over samples of the aforementioned models, to subsequently perform averaging of the vertical components of stress and strain. We use these results to estimate first the *P*-wave modulus and then to compute the normal compliance and reflectivity of the primary fracture. Our results show that both the compliance and reflectivity of the primary fracture increase by more than one order-of-magnitude with respect to the reference model. These findings point to a very significant enhancement of the seismic visibility of large fractures due to FPD with connected secondary ones.

Key words: Fracture and flow; Permeability and porosity; Numerical modelling; Geomechanics; Acoustic properties; Body waves..

1 INTRODUCTION

Fractures are ubiquitous throughout the Earth's upper crust and, in particular, larger-scale fractures tend to dominate the mechanical and hydraulic propreties of the embedding rock masses (e.g. Liu 2005; Jaeger *et al.* 2007). For instance, preferential flow, which is a common occurrence in fractured rocks (e.g. Tsang & Neretnieks 1998; Faulkner *et al.* 2010), is, as simulations suggest, further enhanced by the presence of large fractures (e.g. De Dreuzy *et al.* 2001; Hyman *et al.* 2016). These computational findings are supported by field evidence, which shows that high-permeability zones are often dominated by large fractures, which, in turn, are commonly interconnected to a network of smaller fractures (e.g. Sausse & Genter 2005; Vidal *et al.* 2017). Similary, large fractures can accentuate rock deformation. Laboratory experiments and field observations suggest that fracture compliance scales with fracture length (Worthington & Lubbe 2007; Hobday & Worthington 2012). This implies

*Now at: The Department of Geophysics, Colorado School of Mines, Golden, CO 80401, USA.
†Now at: SINTEF Industry, Trondheim, Norway.
‡Now at: YPF Tecnología S.A. (Y-TEC) Buenos Aires, Argentina.

that large open fractures tend to be more compliant and, hence, deform more readily than smaller fractures. The numerical analysis performed by Morris *et al.* (2017) supports the scaling of compliance with fracture length, although their results show that fracture compliance also depends on the confining stress. Since large fractures tend to control the mechanical and hydraulic properties of the embedding rock masses, their characterization is of great interest for a wide range of applications, such as geothermal energy extraction, CO_2 storage, ground water management, oil and gas exploration and nuclear waste storage, among others.

From a seismic perspective, fractures are deemed large when their size is much greater than the dominant wavelength and act as first-order discontinuities governing the reflection and transmission of impinging seismic waves (e.g. Schoenberg 1980; Pyrak-Nolte *et al.* 1990; Fang *et al.* 2013). Seismic reflection methods are useful tools for fracture characterization due to the generally high reflectivity that large open fractures exhibit as a consequence of their strong mechanical constrast with respect to their embedding background. In fact, multiple studies show that the reflected seismic signals from a fracture plane correlate with the ratio of the fracture compliance to the seismic impedance of the background as well as with the dominant frequency of the seismic wave (e.g. Pyrak-Nolte *et al.* 1990; Liu *et al.* 1995; Gu *et al.* 1996). Relevant examples of seismic reflection applications for fracture characterization are the inversion of fracture compliance from angle-dependent reflection data (e.g. Minato & Ghose 2016; Cui *et al.* 2017) as well as the estimation of fracture properties from the scattered wavefield generated by the spatial heterogeneities of the fracture under study (e.g. Minato & Ghose 2014). However, these and similar methodologies have been largely developed within an elastic framework, which cannot account for fluid–solid interactions prevailing in fractured rocks (e.g. Chapman 2003; Müller *et al.* 2010; Rubino *et al.* 2014). Addressing such problems from a poroelastic perspective therefore allows for a more realistic description of the governing physical processes.

The works of Rubino *et al.* (2015), Barbosa *et al.* (2017), and Wang *et al.* (2017) show that poroelastic effects between fractures and their embedding porous background produce a frequency-dependent behaviour of the normal compliance of the fractures. In fact, the experimental work of Nakagawa (2013) had already evidenced this behaviour. In this work, the author uses samples of water-saturated Berea sandstones with artificial through-going fractures. He measures the deformation across the fractures caused by an applied axial stress at different frequencies to obtain the frequency-dependent characteristics of the compliance. His results reveal the dispersive nature of the normal compliance of the fractures. A similar behaviour of the normal compliance of fractures due to poroelastic effects is suggested by a more recent experimental work (Wang *et al.* 2018). Here, the authors measure the *P*-wave velocity of synthetic water-saturated samples containing vertically stacked penny-shaped cracks, where the measurements are performed at a single frequency and at different angles of incidence. Subsequently, they compare the results with two different analytical models. The measured velocites show a better agreement with an analytical model that considers the frequency-dependent behaviour of the normal compliance of the penny-shaped fractures as a consequence of poroelastic effects in comparison to a model that disregards these interactions and represents the fractures as purely elastic interfaces. Similarly, estimations of normal compliance from field measurements also point to the prevalence of poroelastic interactions between fractures and their surroundings, as evidenced by the relatively large imaginary component of the estimated compliance (e.g. Barbosa *et al.* 2019; Zhou *et al.* 2022). Furthermore, poroelastic effects between a fracture and its embedding background also impact the behaviour of the fracture reflectivity causing its general increase in the seismic frequency range (Nakagawa & Schoenberg 2007; Barbosa *et al.* 2016).

Poroelastic effects on the reflectivity and compliance of fractures are a direct consequence of wave-induced fluid pressure diffusion (FPD) that takes place when seismic waves induce pressure gradients due to the mechanical contrast between the fracture and its embedding background (e.g. Müller *et al.* 2010). FPD increases the normal compliance of fractures, and thus their seismic reflectivity, as the stiffening fluid exits the fracture to equilibrate the pressure (Rubino *et al.* 2015; Barbosa *et al.* 2017). However, in many fractured environments of interest, the background is largely impermeable within the seismic frequency range, which prevents FPD to take place. Conversely, there is far-reaching evidence indicating the pervasive presence of damage zones surrounding large fractures and faults (e.g. Kim *et al.* 2004; Faulkner *et al.* 2010; Savage & Brodsky 2011), which enhance the permeability around the fracture and, thus, provide the necessary conditions for FPD to prevail (e.g. Mitchell & Faulkner 2012; Sotelo *et al.* 2021). Damage zones predominantly consist of a network of fractures at different scales, with a decaying density from the fault core (e.g. Chester *et al.* 2004; Mitchell & Faulkner 2009). Indeed, there is evidence to suggest that secondary fractures intersecting the primary fault are a quite common occurrence. For instance, Bruhn *et al.* (1994) show that multiple episodes of fracturing and thermal alteration tend to create complex secondary fracture patterns in normal fault zones, which notably include mesoscale fractures intersecting a primary macroscale fracture at rather steep angles. Similarly, the studies of Gudmundsson *et al.* (2001) of a fluid-alterated transform fault zone demonstrate the presence of veins striking subparallel and subperpendicular to the fault. Core and borehole measurements examined by Vidal *et al.* (2017) and Glaas *et al.* (2021) show the presence of permeable fractures associated with a hydrothermally alterated normal fault zone. Many of these secondary fractures strike subparallel to the fault but dip, often quite steeply, in an opposing direction, and, thus, establish mechanical and hydraulic connections with the primary fault.

Studies that investigate fracture-to-fracture FPD have so far mainly focused on mesoscale fractures, which are much larger than the pore size but much smaller that the dominant wavelength. In these studies, the main objective has been to investigate the effective seismic response of the fractured rock mass associated with the network properties, such as fracture density, fracture length, degree of fracture connectivity and fluid saturation, among others (e.g. Rubino *et al.* 2013, 2014; Hunziker *et al.* 2018; Solazzi *et al.* 2020). Conversely, FPD effects between a single large fracture and connected mesoscale secondary fractures as well as its impact on the compliance and reflectivity of the large fracture are as of yet largely unexplored. Nonetheless, it is expected that, in particular, a *P*-wave impinging normally onto a large fracture will preferentially increase the fluid pressure inside this fracture rather than in the connected secondary ones due to its more favourable orientation for FPD (e.g. Rubino *et al.* 2014; Guo *et al.* 2017). Furthermore, due to the commonly very high permeability of large fractures, there should be sufficient time for FPD to take place with the connected secondary fractures, thus reducing the stiffening effect induced by the saturating fluid. This further implies that the deformation of large fractures that are interconnected to secondary

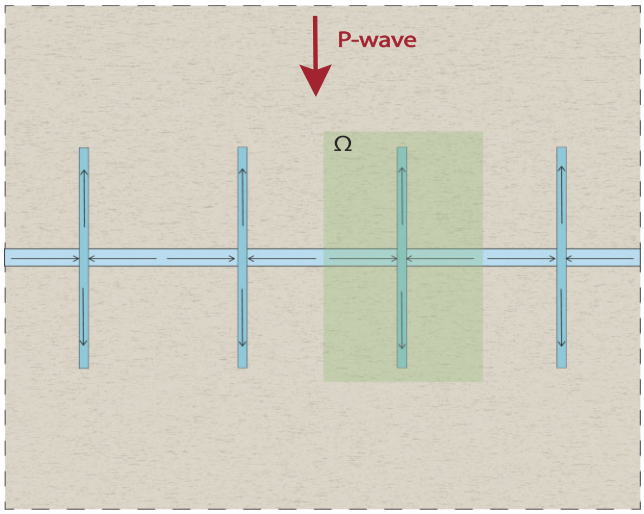

Figure 1. Schematic illustration of a fracture system composed of an infinite horizontal primary fracture connected to equally spaced vertical mesoscale secondary fractures embedded in a background deemed impermeable at the frequencies of interest. The inserted box represents a sample Ω used to estimate the *P*-wave modulus and the corresponding normal compliance of the primary fracture. The thick downward arrow indicates the direction of propagation of an incoming *P*-wave and the thin arrows inside the fractures depict the fluid flow induced by FPD during the compressive cycle of the seismic perturbation.

ones should be more significant than that of their isolated counterparts, and, consequently, their compliance and their reflectivity should be correspondingly higher. In this work, we seek to test the aforementioned hypothesis regarding FPD effects between a large primary fracture and intersecting secondary mesoscale fractures. To this end, we consider several canonical models that consist of an infinite horizontal primary fracture connected to multiple vertical mesoscale fractures. We assume that this fracture system is embedded in a background deemed impermeable for the frequencies of interest (Fig. 1). We evaluate the sensitivity of the primary fracture compliance and its normal-incidence P-wave (PP) reflectivity to variations in the properties of the secondary fractures, such as their lengths, spacings and mechanical moduli. For comparison, we also evaluate the normal compliance and reflectivity of an isolated infinite horizontal fracture.

2 THEORY AND METHODS

In this section, we first present the considered fracture model in the context of Biot's theory of poroelasticity (Biot 1962). Then, we discuss the the physical aspects that constrain the validity of the FPD mechanism in describing wave-induced fluid flow between a large primary fracture and intersecting mesoscale secondary fractures. We also describe the pressure relaxation process associated with FPD, which results in the frequency-dependent behaviour of the seismic properties of the large primary fracture. We then present a homogenization method that permits to isolate the FPD effects on the large primary fracture to estimate its frequency-dependent *P*-wave modulus and normal compliance. Finally, we introduce a simplified model that disregards the presence of the secondary fractures but includes their FPD effect on the large primary fracture through the estimated frequency-dependent *P*-wave modulus. This model is then used to evaluate the normal-incidence PP reflectivity of the primary fracture.

2.1 Poroelastic representation of fractures and fluid pressure diffusion effects

Fractures can be adequately modelled using Biot's theory of poroelasticity (Biot 1962) by representing them as features of a poroelastic continuum characterized by much higher porosities and permeabilities and much lower bulk and shear moduli than the embedding background (e.g. Quintal *et al.* 2014; Rubino *et al.* 2014; Hunziker *et al.* 2018). We consider a model in $\mathbb{R}^2$ comprised of a fracture system embedded in a background deemed impermeable for the frequencies of interest. The fracture system consists of an infinite primary horizontal fracture that is intersected by equally spaced vertical smaller secondary fractures (Fig. 1). Seismic wave propagation in such media can be studied using the Biot's dynamic equations (Biot 1962), which predict the existence of an *S*-wave and a fast and a slow *P* wave. For sufficiently low frequencies, the slow *P*-wave behaves as a FPD process (Dutta & Odé 1979).

We also consider an incoming *P*-wave impinging normally onto the infinite horizontal primary fracture depicted in Fig. 1. The associated wave-induced deformation produces an increase of the pore fluid pressure in the primary fracture, which, in turn, equilibrates by creating fluid flow toward the secondary fractures. For sufficiently low frequencies, which generally comprise the seismic frequency range, this fracture-to-fracture wave-induced fluid flow is driven by FPD (e.g. Müller *et al.* 2010). We are interested in FPD linked to mesoscale secondary fractures since this is particularly relevant for seismic applications (e.g. Pride *et al.* 2004; Müller *et al.* 2010). Mesoscale heterogeneities refer to those that are much smaller than the prodominant wavelength but much greater than the pore size. In Appendix A, we provide further details regarding the constraints related to the scale of the secondary fracture heterogeneities and to the frequencies at which mesoscale FPD prevails. We also describe the associated fluid pressure relaxation process, which produces an equivalent viscoelastic behaviour of the poroelastic medium (e.g. Norris 1993; Pride *et al.* 2004; Rubino *et al.* 2009). For our specific case, the pressure relaxation associated with FPD between the primary and secondary fractures induces a frequency-dependent behaviour of the *P*-wave modulus and of the normal compliance of the primary fracture. We also describe the two limiting pressure regimes, relaxed and unrelaxed, and the corresponding transition zone associated with the pressure relaxation process. We further specify that the transition zone is characterized by a transition frequency f_c, which controls the frequency shift between the relaxed and unrelaxed regimes.

For heterogeneous poroelastic media, the equivalent frequency-dependent moduli can be obtained by applying a numerical homogenization procedure, which consists of solving Biot's (1962) quasi-static equations on a representative sample using pertinent oscillatory tests (e.g. Wenzlau *et al.* 2010; Quintal *et al.* 2011; Rubino *et al.* 2016). In this work, we use a related homogenization procedure of this kind (Sotelo *et al.* 2023) to estimate the frequency-dependent properties of the primary fracture, which we shall outline in the following.

2.2 Homogenization procedure

We consider the model presented in Fig. 1 to estimate the frequency-dependent *P*-wave modulus and the normal compliance of the primary fracture. For the estimation of the properties of the primary fracture, we apply a numerical homogenization procedure based on the work of Sotelo *et al.* (2023), which is characterized by a sampling technique that includes a section of the poroelastic medium together

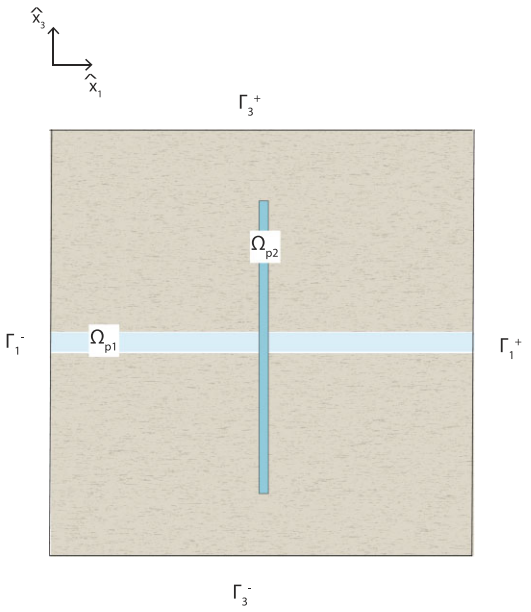

Figure 2. Enlarged view of the sample Ω presented in Fig. 1 consisting of a portion Ω_{p1} of the large primary fracture connected to a secondary fracture Ω_{p2} and the associated section of the embedding background. Γ is the boundary of the sample with $\Gamma = \Gamma_1^+ \cup \Gamma_1^- \cup \Gamma_3^+ \cup \Gamma_3^-$. The secondary fracture is centred in the sample and the sample has a width that is equal to the spacing between consecutive secondary fractures.

with the embedding background. This technique permits to naturally incorporate the boundary conditions (BC) of the embedding background, which is an important criterion when the poroelastic medium is not periodic as in this case. Hence, following Sotelo *et al.* (2023), we take a sample Ω of the model shown in Fig. 1, which consists of a representative part of the fracture system and the embedding background (Fig. 2). The representative part of the fracture system is composed of a portion of the poroelastic primary fracture Ω_{p1} connected to a vertical mesoscopic secondary fracture Ω_{p2}. The secondary fracture is centred in the sample and the sample's width is equal to the spacing between the secondary fractures. Then, we solve Biot's quasi-static equations (Biot 1962) for displacements and pressures over the sample Ω across several frequencies. To find the solutions, we impose periodic BC including a vertical compressional oscillatory test, which produces a deformation similar to that one induced by a *P*-wave impinging normally onto the primary fracture. To isolate the FPD effects on the primary fracture, we compute the average of the vertical stress and strain components over this fracture. Finally, these averages are used to calculate the frequency-dependent *P*-wave modulus and normal compliance of the primary fracture. Further details of this homogenization procedure are given in Appendix B. The overall goal of this homogenization is to consider only the presence of the primary fracture in the reflectivity calculations. It is possible to disregard the secondary fractures because their effect due to FPD with the primary fracture is incorporated in the frequency-dependent properties of the latter.

2.3 Normal-incidence *P*-wave reflectivity of the primary fracture

We consider a simplified model in $\mathbb{R}^1$ as shown in Fig. 3. In this model, the primary fracture is represented by a viscoelastic layer Ω_v characterized by the frequency-dependent *P*-wave modulus obtained through the previously described homogenization procedure.

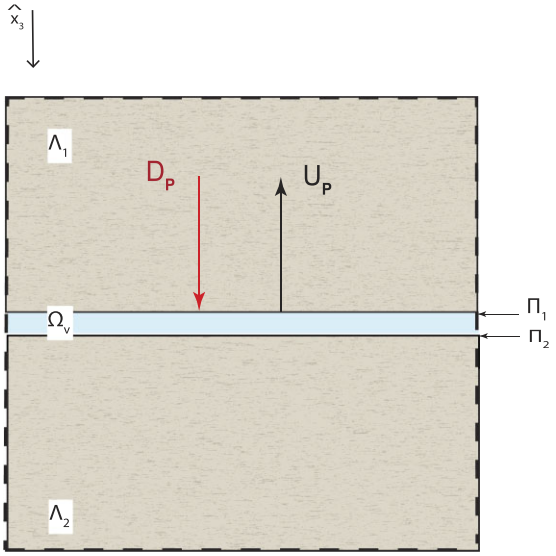

Figure 3. Simplified 1-D model of the primary fracture (Fig. 1), which is represented by a viscoelastic thin layer Ω_v. In this model, the secondary fractures are disregarded but their influence is included in the viscoelastic nature of the primary fracture. The embedding background is represented by the elastic half-spaces Λ_1 and Λ_2 with the same rock physical properties as those considered for the embedding background in Fig. 1. We use this model to compute the PP reflectivities at normal incidence at the the interface Π_1 between the primary fracture Ω_v and the upper half-space Λ_1. The downward arrow represents the incoming *P* wave, while the upward arrow designates the reflected *P* wave.

In this way, we account for the FPD effects on the primary fracture induced by the presence of the secondary fractures. The primary fracture is embedded between the elastic half-spaces Λ_1 and Λ_2 (Fig. 3), which have the same rock physical properties as the embedding background depicted in Fig. 1. In summary, we have further idealized the initial model presented in Fig. 1 to the one shown in Fig. 3, which disregards the presence of the secondary fractures. This is possible because we consider a *P*-wave propagating normally to the plane of the primary fracture. Under this scenario, the propagating wave will mostly be affected by changes in the *P*-wave modulus of the primary fracture due to the FPD interactions with the secondary fractures. Conversely, the secondary fractures are unlikely to affect the *P*-wave propagation not only because their planes are parallel to the direction of the propagation but also because their sizes are very small compared to the dominant wavelength (e.g. Rubino *et al.* 2014; Song *et al.* 2020). As stated before, we assume an incoming *P*-wave impinging normally on the interface Π_1 between the upper elastic half-space and the viscoelastic fracture (Fig. 3). To solve for the PP-reflection coefficients at this interface, we propose plane-wave solutions for the elastic and viscoelastic media, respectively. Then, to find the corresponding amplitudes, we assemble a set of linear equations by imposing continuity of displacements and tractions. The details of this procedure are described in Appendix C.

3 RESULTS

In the following, we present a sensitivity analysis where we vary the geometrical and physical properties of the secondary fractures to investigate their impact on the normal compliance and reflectivity of the primary fracture. We compare the results against those obtained in absence of secondary fractures. In this case, the primary fracture behaves as hydraulically isolated and, hence, can be treated as being

Table 1. Reference values of the physical properties of the primary and secondary fractures as well as of the background (Fig. 1).

Property	Primary fracture (f)	Secondary fracture (h)	Background rock
Grain bulk modulus K_s (GPa)	37	37	37
Porosity ϕ	0.8	0.9	0.015
Frame bulk modulus K_m (GPa)	0.004	0.008	37
Frame shear modulus μ (GPa)	0.002	0.004	29
Permeability κ (D)	1250	1250	10^{-12}
Aperture a (m)	0.001	0.001	NA
Length L (m)	infinite	3.04	NA
Spacing s (m)	NA	3.2	NA
Grain density ρ_s (kg m^{-3})	2730	NA	2730

Table 2. Reference values of the physical properties of pore fluids.

Property	Water	Gas
Fluid density ρ_f (kg m^{-3})	1000	78
Fluid bulk modulus K_f (GPa)	2.25	0.012
Fluid viscosity η (Pa.s)	10^{-3}	1.5×10^{-4}

elastic for the evaluation of its compliance and reflectivity. The normal compliance of this elastic fracture is the so-called undrained normal compliance and its reflectivity is calculated by applying a similar procedure to the one described in Appendix C but, for this case, we consider that the fracture is represented by an elastic thin layer instead of a viscoelastic one. Consequently, the applied governing and the constitutive equations are those as detailed in eqs (C1) and (C2) of Appendix C.

Table 1 shows the rock physical properties for the primary fracture, secondary fractures and the background, respectively. Table 2 lists the properties of the considered pore fluids. Unless stated otherwise, we assume that the pores of the primary and secondary fractures are water-saturated. We remark that the grain and frame bulk moduli of the background are equal. This yields a Biot–Willlis effective stress coefficient α equal to zero, which implies that the pore fluid pressure does not have any effect on the total stress (eq. B2 of Appendix B). Moreover, the background permeability is so low (10^{-12} D) that it can be regarded as impermeable for the typical seismic frequency range. In summary, due to its assigned properties, the background behaves effectively as an elastic medium. To obtain both the frequency-dependent P-wave modulus and normal compliance of the primary fracture for the different tested models, we apply the homogenization procedure described in the previous section using a square sample Ω (Fig. 2) with a side length of 3.2 m. This homogenization procedure is valid for frequencies that are much lower than Biot's characteristic frequency (eq. A1 of Appendix A). The corresponding values for the primary and secondary fractures are 103.2 and 116.1 Hz, respectively, which are at the high-end of the standard exploration seismic frequency range. Although the upper limit of the seismic band is, for practical purposes, within the same order-of-magnitude of the computed Biot's characteristic frequencies, we can still consider that the results obtained under the FPD assumption are valid. The reason for this is that a smooth transition is expected from the FPD mechanism characterized by a viscous-dominated solid–fluid drag forces toward a wave-induced fluid flow mechanism controlled by an inertia-dominated drag (Rubino *et al.* 2014). Thus, the results we present in the following are considered valid for frequencies up to ~100 Hz. Nonetheless, we present them up to 1 kHz for illustration purposes.

In the following, we analyse plots of the ratio of the frequency-dependent fracture normal compliance $Z_N(\omega)$ and its undrained value Z_N^u, that is Z_N ratio $= Z_N(\omega)/Z_N^u$. The undrained normal compliance Z_N^u designates the minimum theoretical value that $Z_N(\omega)$ can take, which corresponds to its unrelaxed regime. We remark that in this regime the primary fracture behaves as hydraulically isolated from the secondary ones. The undrained normal compliance is calculated as $Z_N^u = a_f/H$, where $H = H_d + M\alpha^2$ is the undrained P-wave modulus and H_d is the drained P-wave modulus, respectively, with $H_d = \lambda_d + 2\mu$. The remaining physical properties are defined in eq. (B3) of Appendix B. Using the properties for the primary fracture from Table 1, we find that $Z_N^u = 3.6 \times 10^{-13}$ m Pa^{-1}. Conversely, the drained normal compliance Z_N^d denotes maximum theoretical value that $Z_N(\omega)$ can take if it were possible to drain all the pore fluid from the primary fracture. The drained normal compliance is calculated as $Z_N^d = a_f/H_d$. Using again the properties for the primary fracture from Table 1, we find $Z_N^d = 1.5 \times 10^{-10}$ m Pa^{-1}. However, it is expected that the magnitude of the relaxed $Z_N(\omega)$ is lower than the drained one since the secondary fractures provide a limited pore volume to drain the fluid from the primary fracture. Finally, the theoretical maximum Z_N^{max} ratio prevails when $Z_N(\omega) = Z_N^d$, which yields $Z_N^{max} = Z_N^d/Z_N^u = 416.5$.

3.1 Sensitivity to the geometrical properties of the secondary fractures

In this subsection, we investigate the sensitivity of the normal compliance and reflectivy of the primary fracture to variations in the geometrical properties of the secondary fractures, such as their length L^h, aperture a^h and spacing s^h. Here, the superscript h refers to the secondary fractures. To perform this sensitivity analysis, we modify one parameter at a time by repeatedly halving its value to a maximum eight-fold decrement with regard to its reference value (Table 1). We remark that the decrease in length of the secondary fractures produces the same reduction of their pore volume from the reference case as the corresponding decrease in their aperture does. In contrast, the decrease in spacing of the secondary fractures produces an increment of their pore volume with respect to the reference case.

Fig. 4 presents the Z_N ratio as a function of frequency for the different geometrical parameters of the secondary fractures. The results show that there is an increase of the normal compliance of the primary fracture with respect to its unrelaxed value (Z_N ratio of 1) for all tested parameters of the secondary fractures. This is the consequence of FPD with the secondary fractures prevailing in regimes other than the unrelaxed one. Specifically, at sufficiently low frequencies, the Z_N ratio shows a constant maximum for each tested value as the result of FPD occurring in the relaxed regime.

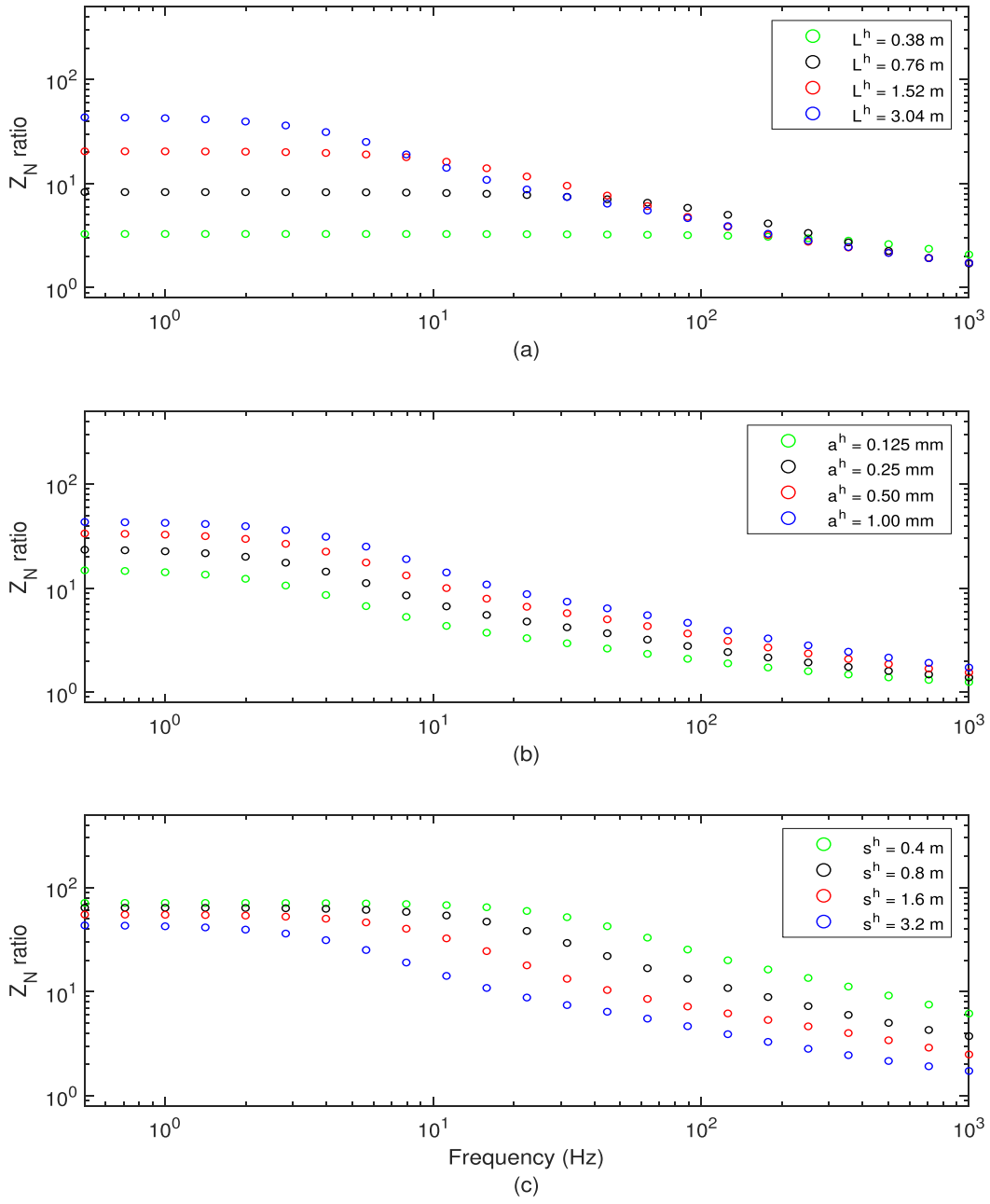

Figure 4. Ratio of the frequency-dependent normal compliance of the primary fracture to its undrained compliance (Z_N ratio) as a function of frequency considering secondary fractures of varying (a) lengths L^h, (b) apertures a^h and (c) spacings s^h. Equal colours in (a) and (b) denote equal pore volumes of the corresponding secondary fractures.

Consequently, we denote this Z_N ratio as the relaxed one. We remark that, the theoretical upper limit of the relaxed Z_N ratio is the one associated with the drained compliance of the primary fracture, which, as previously mentioned, is equal to 416.5. As the frequency increases, the transitional FPD regime prevails, which induces the monotonic decrease of the Z_N ratio toward its unrelaxed value. The results show that the relaxed Z_N ratio increases with increasing magnitudes of the length L^h and aperture a^h of the secondary fractures and with decreasing values of their spacing s^h. The largest relaxed Z_N ratio of 71.2 corresponds to the minimum spacing of 0.4 m of the secondary fractures (Fig. 4c). This spacing is associated with the greatest pore volume increase of the secondary fractures with regard to the reference case.

These results also show that, in the relaxed regime, secondary fractures with equivalent pore volumes but different geometrical configurations, with regard to their length and aperture, induce the flow of different volumes of fluid from the primary fracture (Figs 4a and b). Shorter secondary fractures allow for less fluid to flow from the primary fracture than narrower ones. This, in turn, produces a lower increase of the associated relaxed Z_N ratio of the primary fracture. A possible explanation for this effect is the smaller frame deformations induced in shorter secondary fractures compared to those produced in narrower ones.

Besides, these results show that the sensitivity of the relaxed Z_N ratio is different for each of the tested geometrical properties of the secondary fractures. The relaxed Z_N ratio is most sensitive

to variations in length L^h of the the secondary fractures (Fig. 4a) and is least sensitive to variations in their spacing s^h (Fig. 4c). An intermediate sensitivity is associated with variations in their aperture a^h (Fig. 4b). Specifically, the relaxed Z_N ratio shows an increase of ∼13-fold, from 3.3 to 43.5, for the corresponding eight-fold increase in length L^h. Then, the relaxed Z_N ratio increases close to three-fold, from 15.0 to 43.5, for an eight-fold aperture a^h increase. Finally, the relaxed Z_N ratio presents the lowest increase of ∼1.5-fold, from 43.5 to 71.2, in response to an eight-fold decrease in spacing s^h. The higher sensitivity of the relaxed Z_N ratio to variations in length of the secondary fractures can be associated to a higher deformation or strain induced on these fractures per variation of unit length, which allows for greater fluid volume to flow from the primary fracture. This effect of the strain on the relaxed Z_N ratio can be deduced from eqs (B7) and (B8) of Appendix B.

On the other hand, the considered properties of the secondary fractures influence differently the characteristic transition frequency f_c of the primary fracture normal compliance. For instance, f_c presents the highest sensitivity to changes in length L^h of the secondary fractures (Fig. 4a), showing decreasing values from ∼ 1.0 kHz to ∼ 5.6 Hz as L^h increases. In contrast, f_c is the least sensitive to changes in the aperture a^h of the secondary fractures (Fig. 4b). In this case f_c, takes increasing values from ∼4.0 to ∼ 5.6 Hz as a^h increases. Finally, f_c presents an intermediate sensitivity to the spacing s^h of the secondary fractures (Fig. 4c), where it decreases from ∼44.6 to ∼5.6 Hz with increasing spacing. According to eqs (A4) and (A5) of Appendix A, f_c is directly proportional to the fractional volume β occupied by the fractures but inversely proportional to their size squared l_h^2. This points to a trade-off between these two parameters since an increase in their size will also increase their fractional volume. However, their overall effect on f_c will depend on their relative magnitudes. A geometric increase either in the length L^h or in the aperture a^h of the secondary fractures produces the same pore volume increase, that is an equal increase of their fractional volume β. Under this scenario, our results reveal that, because of its relative higher magnitude, the increase in length L^h of the secondary fractures tends to dominate f_c, causing its decrease. In contrast, when increasing the aperture a^h of the secondary fractures, it is the increase of their fractional volume β that takes control, increasing, consequently, f_c. Finally, the increase in spacing s^h of the secondary fractures produces a reduction of their fractional volume β while their size remains constant. In this case, as the results show, f_c decreases.

Next, we explore how an increase in normal compliance of the primary fracture as a consequence of FPD effects with the secondary fractures impacts the reflectivity of the primary fracture. Fig. 5 presents the absolute value of normal-incidence PP reflectivities of the primary fracture as a function of frequency for the same geometrical parameters of the secondary fractures presented in Fig. 4. The results show that, for sufficiently low frequencies, the reflectivity of the primary fracture presents a maximum increase from the reference case, which disregards the secondary fracture. This is a consequence of FPD toward the secondary fractures prevailing in the relaxed regime. However, for progressively higher frequencies, the primary fracture reflectivity decreases monotonically toward its elastic limit, which is the result of FPD transitioning toward its unrelaxed state. Regarding the reflectivity of the primary fracture in the relaxed FPD regime, the strongest increase of ∼65-fold is associated with most closely spaced secondary fractures (s^h = 0.4 m in Fig. 5c). The second largest increase in reflectivity of ∼44-fold corresponds to both the largest (L^h = 3.04 m in Fig. 5a) and the widest (a^h = 0.001 m in Fig. 5c) secondary fractures. Regarding the sensitivity of the reflectivity of the primary fracture to changes in the geometrical properties of the secondary fractures, the results show a similar behaviour as the one described for its normal compliance. That is, its reflectivity at normal incidence is most sensitive to changes in length L^h, then aperture a^h, and, finally, spacing s^h.

3.2 Sensitivity to the physical properties of the secondary fractures

In this subsection, we investigate the sensitivity of the normal compliance and the reflectivy of the primary fracture to variations in the physical properties of the secondary fractures, such as their bulk K_m^h and shear μ^h moduli, permeability κ^h and type of pore fluid f^h. To perform this sensitivity analysis, we again modify one parameter at a time, taking as the reference values the ones specified in Table 1. For the mechanical moduli, we repeatedly double the bulk modulus K_m^h, keeping the ratio K_m^h/μ^h constant and equal to two. To investigate the sensitivity to the permeability κ^h, we repeatedly decrease its value by 50 per cent. Finally, to study the sensitivity to the pore fluid f^h, we compare the results for water or gas as saturating fluids in the secondary fractures, while the primary fracture remains water-saturated.

Fig. 6 presents the resulting Z_N ratio as a function of frequency for the different physical properties of the secondary fractures. These results show that the presence of the secondary fractures increases the normal compliance of the primary fracture with respect to its unrelaxed value (Z_N ratio of 1) for frequencies associated with FPD prevailing in regimes other than the unrelaxed one. As remarked in the previous subsection, at sufficiently low frequencies, the relaxed Z_N ratio shows a constant maximum for each of the tested values. This occurs as a consequence of FPD prevailing in the relaxed regime. The largest relaxed Z_N ratio of 150.1 is associated with gas-saturated secondary fractures (Fig. 6c). This is a consequence of the much larger compressibility of gas compared to that of the water, which allows for more fluid to flow from the primary fracture as FPD occurs.

We also observe that the relaxed Z_N ratio shows sensitivity to changes in the bulk modulus K_m^h (Fig. 6a) and in the type of pore fluid f^h (Fig. 6c) of the secondary fractures but not to changes in their permeaility. In fact, Fig. 6(a) shows that the relaxed Z_N ratio increases close to three-fold, from 15.9 to 43.5, which corresponds to an eight-fold decrease in the bulk modulus K_m^h, from 0.064 to 0.008 GPa. These results suggest that more deformable secondary fractures can accommodate larger fluid volumes coming from the primary fracture because their pores can expand more readily. Similarly, Fig. 6(c) shows an increase of ∼3.5-fold in the relaxed Z_N ratio, from 43.5 to 150.1, when changing the saturating pore fluid from water to gas. As previously noted, this increase is the result of the higher compressibility of gas compared to that of water, which permits to accommodate more water flowing from the primary fracture into the pores of the secondary fractures as the gas compresses. However, the relaxed Z_N ratio is insensitive to variations in the permeability of the secondary fractures (Fig. 6b). That is, for all tested permeabilities κ^h, the relaxed Z_N ratio remains unchanged. The only effect that permeability has is with regard to the characteristic transition frequency of the primary fracture compliance as described below.

Regarding the sensitivity of the characteristic transition frequency f_c of the normal compliance of the primary fracture, our results show that f_c increases from ∼5.6 to ∼15.8 Hz as the bulk

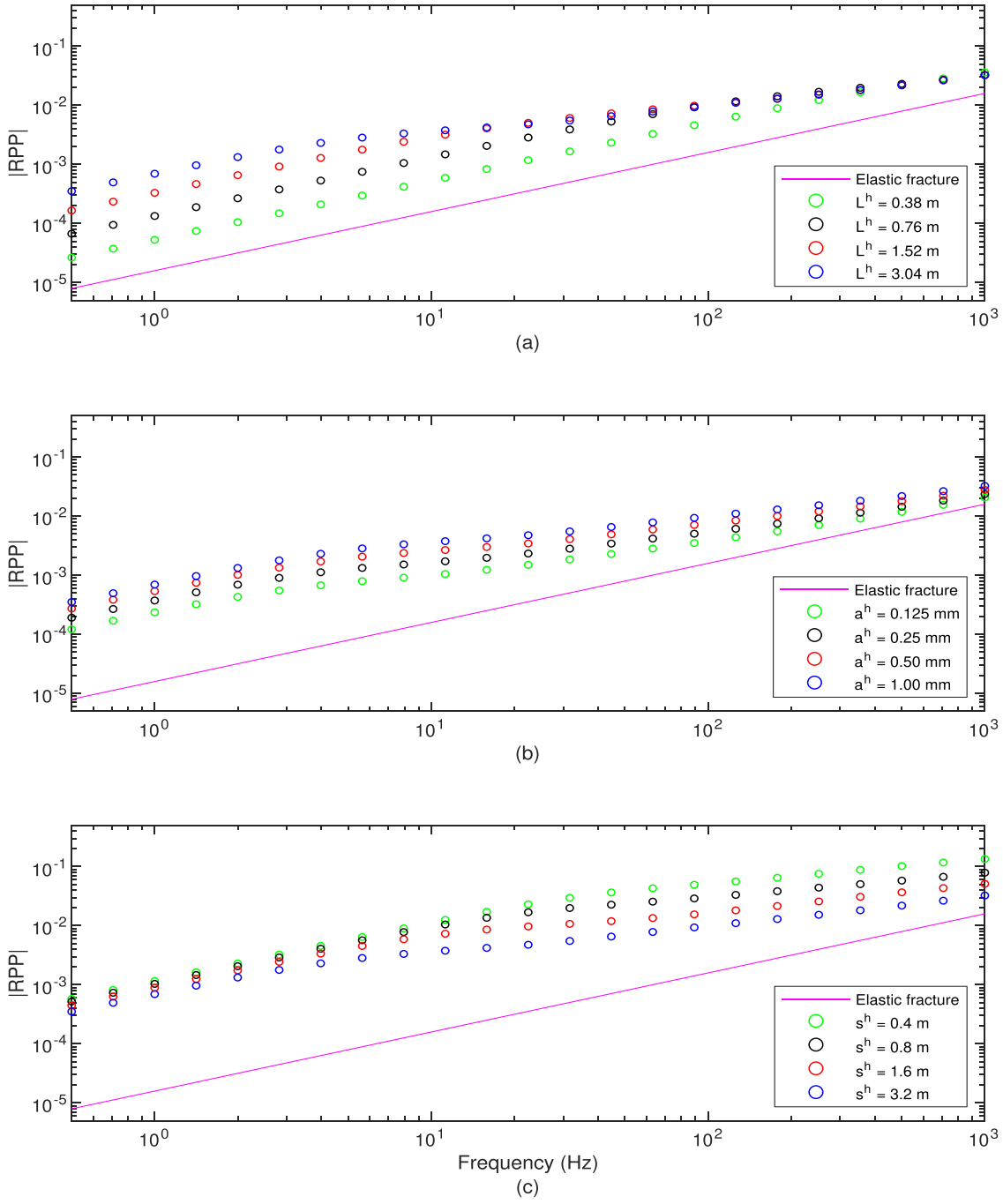

Figure 5. Absolute value of normal-incidence *P*-wave reflection coefficients as a function of frequency considering different frequency-dependent *P*-wave moduli of the primary fracture. These moduli include the effect of FPD interactions with secondary fractures of varying (a) lengths L^h, (b) apertures a^h and (c) spacings s^h as shown in Fig. 4. For comparison, we also show the reflectivity of a primary fracture in absence of secondary fractures, which corresponds to an elastic one.

modulus K_m^h increases. Similarly, we observe that f_c increases from ∼1.4 to ∼5.6 Hz as the permeability κ^h increases. Finally, f_c decreases from ∼5.6 to ∼2.8 Hz when the saturating fluid f^h changes from water to gas. According to eqs (A4) and (A5) of Appendix A, f_c should increase as the permeability κ^h of the secondary fractures increases and as the viscosity η of the saturating fluid f^h decreases, which agrees with the described results. However, the effect of the bulk modulus K_m^h of the secondary fractures on f_c is difficult to predict using the aforementioned equations because K_m^h is used in the calculation of several effective parameters of the fractured medium as the Biot's storage fluid modulus M^m, the drained H_d^m and the low-frequency H_s^m *P*-wave moduli, which, in turn, impact f_c either in a direct or inverse manner.

Fig. 7 shows that the reflectivity of the primary fracture has a similar response to that of its associated normal compliance due to FPD effects with the secondary fractures. We observe that, at sufficiently low frequencies, there is a maximum increase of the primary fracture reflectivity with respect to its elastic references

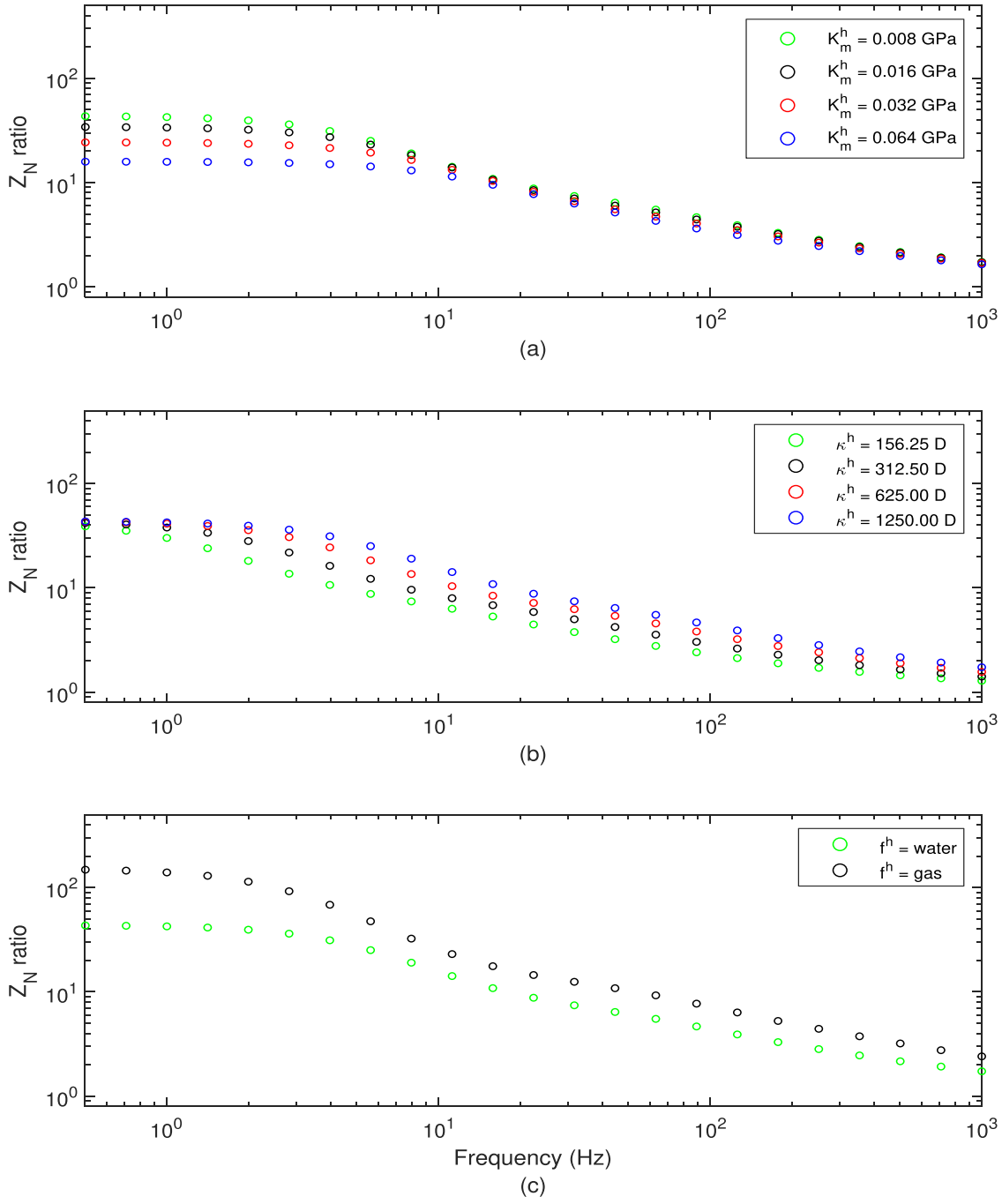

Figure 6. Ratio of the primary fracture normal compliance to its undrained value (Z_N ratio) as a function of frequency considering secondary fractures with different (a) bulk moduli K_m^h, (b) permeabilities κ^h and (c) pore fluids f^h.

as a consequence of FPD with the secondary fractures prevailing in the relaxed regime. Specifically, our results show that the largest increase of the reflectivity of the primary fracture of close to 1.5-orders-of-magnitude is associated with gas-saturated secondary fractures (Fig. 7c). Similary, the second largest reflectivity increase of ∼44-fold is associated with the softest secondary fractures (K_m^h = 0.008 GPa in Fig. 7a) and with any of the tested permeabilities of the secondary fractures (Fig. 7b). This lack of sensitivity of the reflectivity of the primary fracture in the relaxed regime to changes of the permeability of the secondary fractures is consistent with the corresponding results for its compliance (Fig. 6b).

3.3 Summary of the sensitivity analyses

In this subsection, we provide an analysis regarding the effect that the geometrical and physical properties of the secondary fractures have on the normal compliance of the primary fracture at its relaxed state and on the corresponding characteristic transition frequency f_c. To this end, Fig. 8 presents the Z_N ratio of the primary fracture associated with its relaxed state (relaxed Z_N ratio) versus the transition frequency f_c of its normal compliance for all of the previously tested properties of the secondary fractures. We further remark that the relaxed Z_N ratio reflects the maximum increase that the normal fracture compliance can attain with respect to its unrelaxed

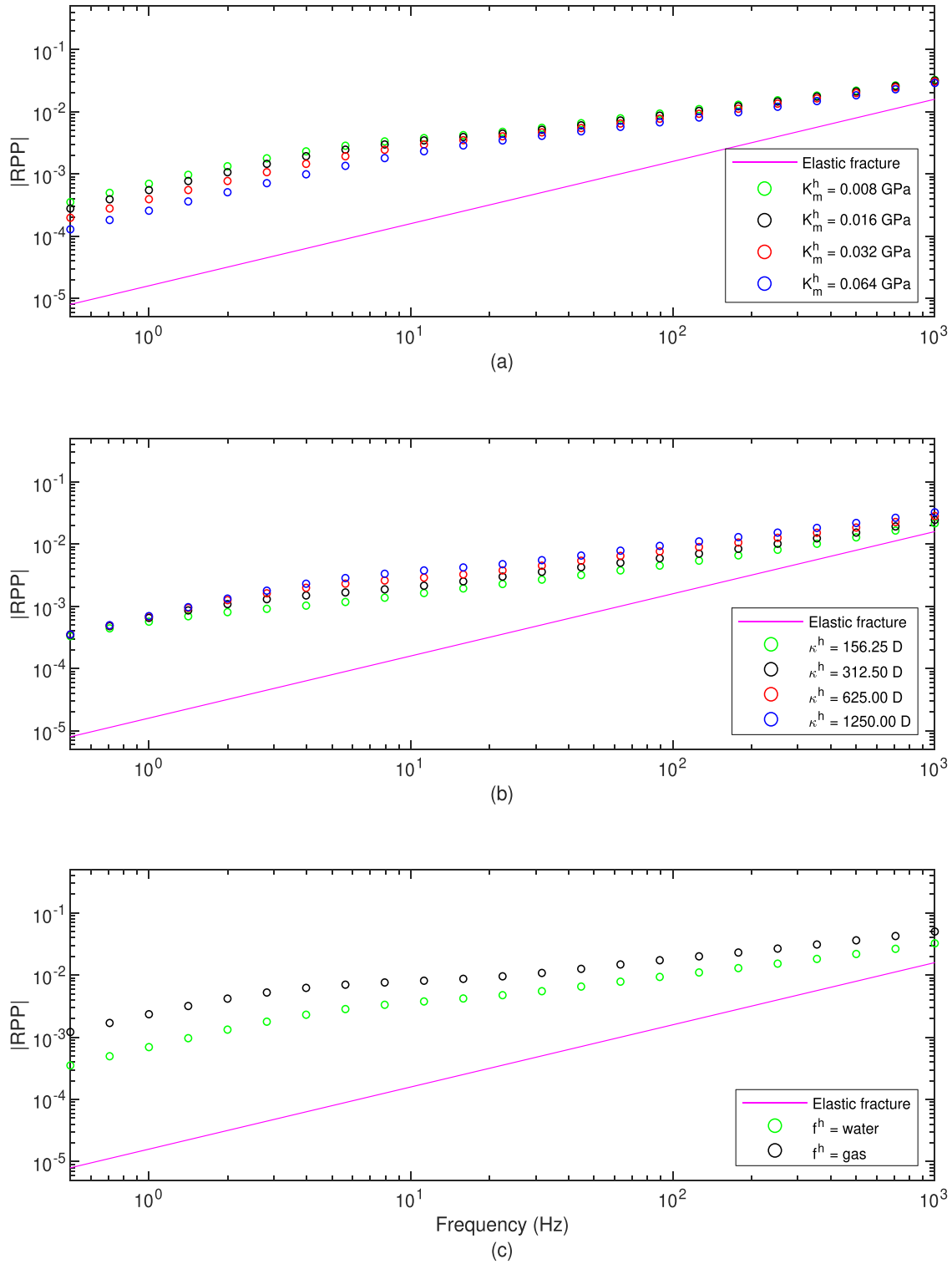

Figure 7. Absolute value of normal-incidence *P*-wave reflection coefficients as a function of frequency considering different frequency-dependent *P*-wave moduli of the primary fracture. These moduli include the effect of FPD interactions with secondary fractures with different (a) bulk moduli K_{m}^{h}, (b) permeabilities κ^{h} and (c) pore fluids f^{h}. For comparison, we also show the reflectivity curve of an isolated, that is, elastic, primary fracture.

value for a given set of secondary fracture parameters (Figs 4 and 6).

The results show that, overall, the relaxed Z_{N} ratio is most sensitive to changes in the length L^{h} of the secondary fractures, with an increase of ∼13-fold, from 3.3 to 43.5, for an eight-fold increase of the length L^{h}. This is followed by the the impact of changing the saturating pore fluid of the secondary fractures from water to gas, which produces an increase of the relaxed Z_{N} ratio of the primary fracture of ∼3.5-folds, from 43.5 to 150.1. Next, the changes in the bulk moduli K_{m}^{h} and in the aperture a^{h} of the secondary fractures have a similar impact on the sensitivity of the relaxed Z_{N} ratio. That is, an eight-fold decrease in the bulk modulus and

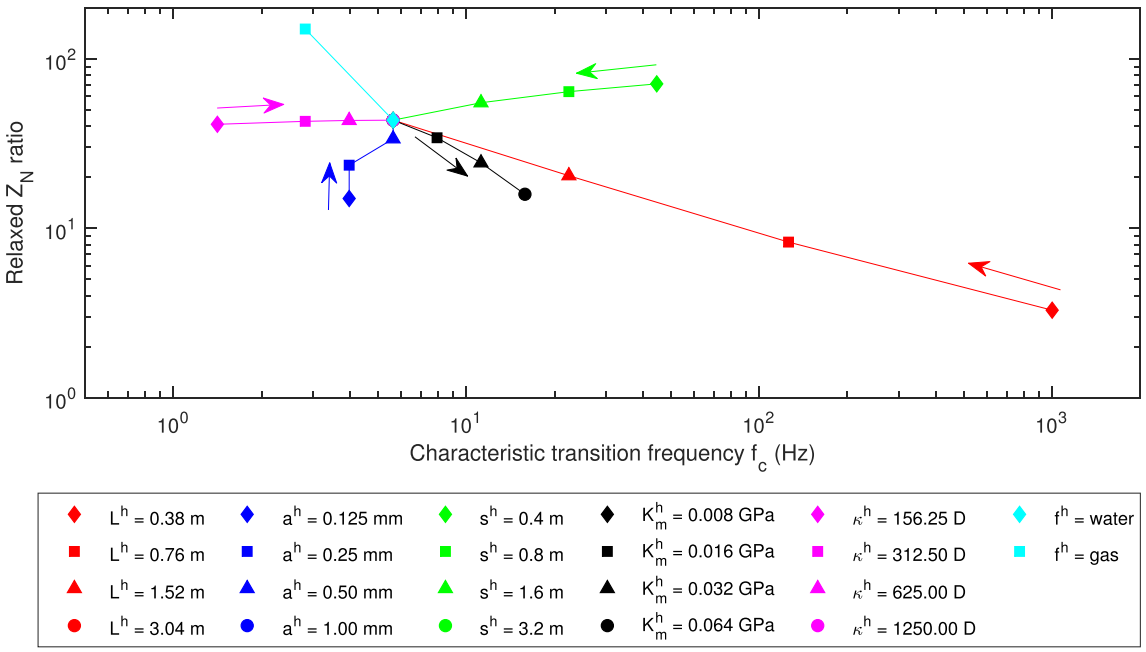

Figure 8. Relaxed Z_N ratio of the primary fracture as a function of the characteristic transition frequency f_c of its normal compliance for the different properties of the secondary fractures (Figs 4 and 6). The arrows point toward the direction in which the properties of the secondary fractures increase in magnitude.

a similar increase in the aperture generate close to three-fold increase in the corresponding relaxed Z_N ratio, from ∼16 to 43.5. The spacing s^h of the secondary fractures has a much lower impact than the aforementioned properties on the sensitivity of the relaxed Z_N ratio, where an eight-fold decrease of spacing produces roughly a doubling of the the relaxed Z_N ratio, from 43.5 to 71.2. Finally, as previously stated, changes in the permeability κ^h of the secondary fractures do not have any impact on the relaxed Z_N ratio.

Changes in permeability of the secondary fractures affect the transition frequency f_c of the normal compliance of the primary fracture. Higher permeabilities increase its transition frequency in agreement with eqs (A4) and (A5) of Appendix A. Our results also show a similar direct relationship of f_c with the bulk modulus K_m^h of the secondary fractures. Conversely, we observe an inverse relationship of f_c with the length L^h and spacing s^h of the secondary fractures. Indeed, it is possible to verify that f_c decreases linearly with the inverse of the length to the power of 2.5 ($(L^h)^{-2.5}$) and as well as with the inverse of the spacing ($(s^h)^{-1}$), respectively. These results are consistent with eq. (A5) of Appendix A, which predicts an inverse proportionality between the transition frequency and the size of the characteristic heterogeneity, albeit to the power of two ($(l_h)^{-2.0}$). Next, we observe that changes in the aperture a^h of the secondary fractures do not increase f_c in every case. As discussed in Section 3.1, the increase of the fractional volume and aperture of the secondary fractures have opposing effects on f_c (eq. A4 of Appendix A), and their overall impact depends on their relative magnitudes. Finally, we observe that gas-saturated secondary fractures induce a lower transition frequency f_c compared to the water-saturated case. As previously discussed, this is the direct consequence of the lower viscosity of gas compared to that of water (eqs A4 and A5 of Appendix A). The previous sensitivity analyses together with the current results show that the characteristic transition frequency f_c constrains the upper frequency limit up to which the relaxed state of the fracture normal compliance prevails, hence, controlling its seismic visibility. That is, relatively high values of f_c, higher than the upper bound of the seismic frequency range, render the normal fracture compliance in its relaxed state seismically visible. In contrast, lower f_c values can either limit the seismic visibility of the relaxed normal fracture compliance or render it not visible at all. The results also show that f_c is controlled by the fractional volume of the secondary fractures and the relative magnitudes of their geometrical and physical properties, as well as the viscosity of the saturating fluid.

3.4 Effects of correlated properties of the secondary fractures

So far, we have assessed the sensitivity of the normal compliance and reflectivity of the primary fracture to variations in several properties of the secondary fractures. In doing so, the property of interest was incrementally modified, while all other properties were kept constant. Now we shall assume that the properties of the secondary fractures are not independent from each other but directly or indirectly correlated to their length, which is indeed consistent with much of the available observational evidence (e.g. Hatton *et al.* 1994; Renshaw 1995; Bonnet *et al.* 2001; Morris *et al.* 2017).

Following this evidence, we use a power law relationship to estimate the aperture a^h using the length L^h of the secondary fractures (e.g. Hatton *et al.* 1994): $a^h = c_1 (L^h)^{d_1}$, where $c_1 = 10^{-3.4}$ and $d_1 = 1.05$, respectively. We also relate the permeability κ^h of the secondary fractures to their hydraulic aperture H^h through (Zimmerman & Bodvarsson 1996; Jaeger *et al.* 2007): $\kappa^h = (H^h)^2/12$, where the hydraulic aperture is related to the arithmetic mean aperture of the secondary fractures as (Renshaw 1995; Jaeger *et al.* 2007): $(H^h)^3 = (a^h)^3(1 + r^2)^{-1.5}$. In doing so, we assume that the previously estimated aperture a^h is the arithmetic mean aperture

Table 3. Properties of the secondary fractures correlated to their length.

Property	Secondary fracture (h)		
Length L (m)	0.7	1.5	2.9
Aperture a (m)	3×10^{-4}	6×10^{-4}	1.2×10^{-3}
Permeability κ (D)	51.9	257.0	1026.1
Frame bulk modulus K_m (GPa)	0.010	0.012	0.014
Frame shear modulus μ (GPa)	0.006	0.008	0.009
Drained normal compliance Z_N (m/Pa)	1.5×10^{-11}	2.7×10^{-11}	4.5×10^{-11}
Tangential compliance Z_T (m/Pa)	4.3×10^{-11}	7.8×10^{-11}	1.3×10^{-10}

of the secondary fractures and r is the ratio between the corresponding standard deviation and the mean aperture, which we assume to be equal to 11. This value is consistent with observations on natural fractures with pronounced asperities (Renshaw 1995).

It is also possible to relate the bulk K_m^h and shear μ^h moduli of the secondary fractures to their drained normal Z_N^h and tangential Z_T^h compliances (Nakagawa & Schoenberg 2007; Rubino *et al.* 2014): $\mu^h = a^h/Z_T^h$ and $K_m^h = a^h/Z_N^h - 4\,a^h/(3\,Z_T^h)$, where the normal compliance of the secondary fractures can be further related to their length by a power law relationship $Z_N^h = c_2\,(L^h)^{d_2}$, with $c_2 = 10^{-10.7}$ and d_2 =0.77, respectively. This curve follows the trend of the data presented in Barbosa *et al.* (2019). Besides, reported ranges of the ratio Z_N/Z_T for dry fractures are for instance from 0.2 to 0.55 (Lubbe & Worthington 2006) and from 0.2 to 0.77 (Pyrak-Nolte *et al.* 1990; Verdon & Wüstefeld 2013). For this example we consider a Z_N^h/Z_T^h ratio of 0.35 for the secondary fractures. Notice that the relationships for estimating the aperture and permeability of the secondary fractures show a monotonically increasing trend with respect to their length and aperture, respectively.

Table 3 summarizes the geometrical and physical properties for three different secondary fracture lengths considered in this analysis: 0.7, 1.5 and 2.9 m. All other properties are assumed to be the same for all cases and correspond to those listed in Table 1 except for the spacing of the secondary fractures, for which we consider a value of 1.6 m. As expected, the estimated apertures and permeabilities of the secondary fractures increase with their length. For the values considered, the bulk and shear moduli of the secondary fractures also increase with their length. For reference, Table 3 also presents the estimated normal and tangential compliances of the secondary fractures, which show an increasingly compliant behaviour with increasing length. Besides, we assume that both the primary and secondary fractures are water-saturated (Table 2).

Fig. 9 shows the impact that the three different sets of properties of the secondary fractures (Table 3) have on the normal compliance of the primary fracture (Fig. 9a) and on the corresponding PP reflectivity at normal incidence (Fig. 9b) as a function of frequency. Regarding the effects on the normal compliance of the primary fracture, Fig. 9(a) shows that the relaxed Z_N ratio takes progressively larger values of 7.2, 19.7 and 51.6 as the length L^h of the secondary fractures increases. This behaviour suggests that the length of the secondary fractures controls the FPD interactions with the primary fracture despite of their slightly higher bulk modulus. This indicates that longer secondary fractures, which are also associated with larger apertures, provide a greater pore volume and thus permit the drainage of more fluid from the primary fracture during FPD. Fig. 9(a) also shows that the characteristic transition frequency f_c has the same value of 11.2 Hz for the three considered cases. This result implies that the tendency of the progressively longer fractures to decrease f_c (Fig. 4a) is counterbalanced by the opposite effect that the increasing permeabilities have on f_c. We also remark that the relaxed Z_N ratio of 51.6 induced by the longest secondary fractures (2.9 m) is higher than the one obtained in the sensitivity analyses for a secondary fracture length of 3.04 m, for which, the associated relaxed Z_N ratio is 43.5. This higher relaxed Z_N ratio is a consequence of the narrower spacing of the secondary fractures, 1.6 m instead of 3.2 m, which also has an influence on the characteristic transition frequency f_c by increasing its magnitude (Figs 4c and 8).

Fig. 9(b) shows that the absolute value of the PP reflectivity at normal incidence of the primary fracture increases with increasing length L^h of the secondary fractures compared to its elastic reference for frequencies corresponding to FPD regimes other than the unrelaxed one. This reflectivity behaviour is produced by the softening of the normal compliance of the primary fracture that occurs as the secondary fractures lengthen (Fig. 9a). Correspondingly, the maximum increase of the reflectivity of the primaray fracture of ~50-fold is associated with the longest secondary fracture (2.9 m) for frequencies in the relaxed FPD regime.

4 DISCUSSION

4.1 Evidence of FPD effects in fracture zones embedded in largely impermeable environments

The main finding of our work is that FPD between large primary and interconnected smaller secondary fractures embedded in largely impermeable environments enhances the seismic visibility of the former. The reason for this is that FPD effects produce an increase of the compliance of the primary fractures, which, in turn, leads to an increase of their mechanical contrast with respect to the embedding background. In general, reflectivity-based assessments in hard rock environments are quite challenging due to the often low signal-to-noise ratio of such data in conjunction with the typically low impedance contrasts (e.g. Adam *et al.* 2000; Ahmed *et al.* 2015; Cheraghi *et al.* 2021). However, some of these studies show unusually strong reflectors associated with faults and dense fracture zones (e.g. Harjes *et al.* 1997; Bergman *et al.* 2002; Casini *et al.* 2010), which arguably can be best explained by notable FPD effects between connected fractures. For instance, Harjes *et al.* (1997) and Bergman *et al.* (2002) associated imaged reflectors in crystalline rock with a fluid-saturated fracture zone after assessing complementary information from borehole seismic and petrophysical measurements. Further interwell hydraulic communication tests confirmed that fractures in these zones were highly interconnected. A similar analysis was performed by Casini *et al.* (2010) who also associated strong reflectors in crystalline rock with interconnected fractures after performing production tests in several boreholes intersecting the imaged targets. Likewise, the interpretation performed by Szalaiová *et al.* (2015) of strong seismic reflections in the upper crystalline

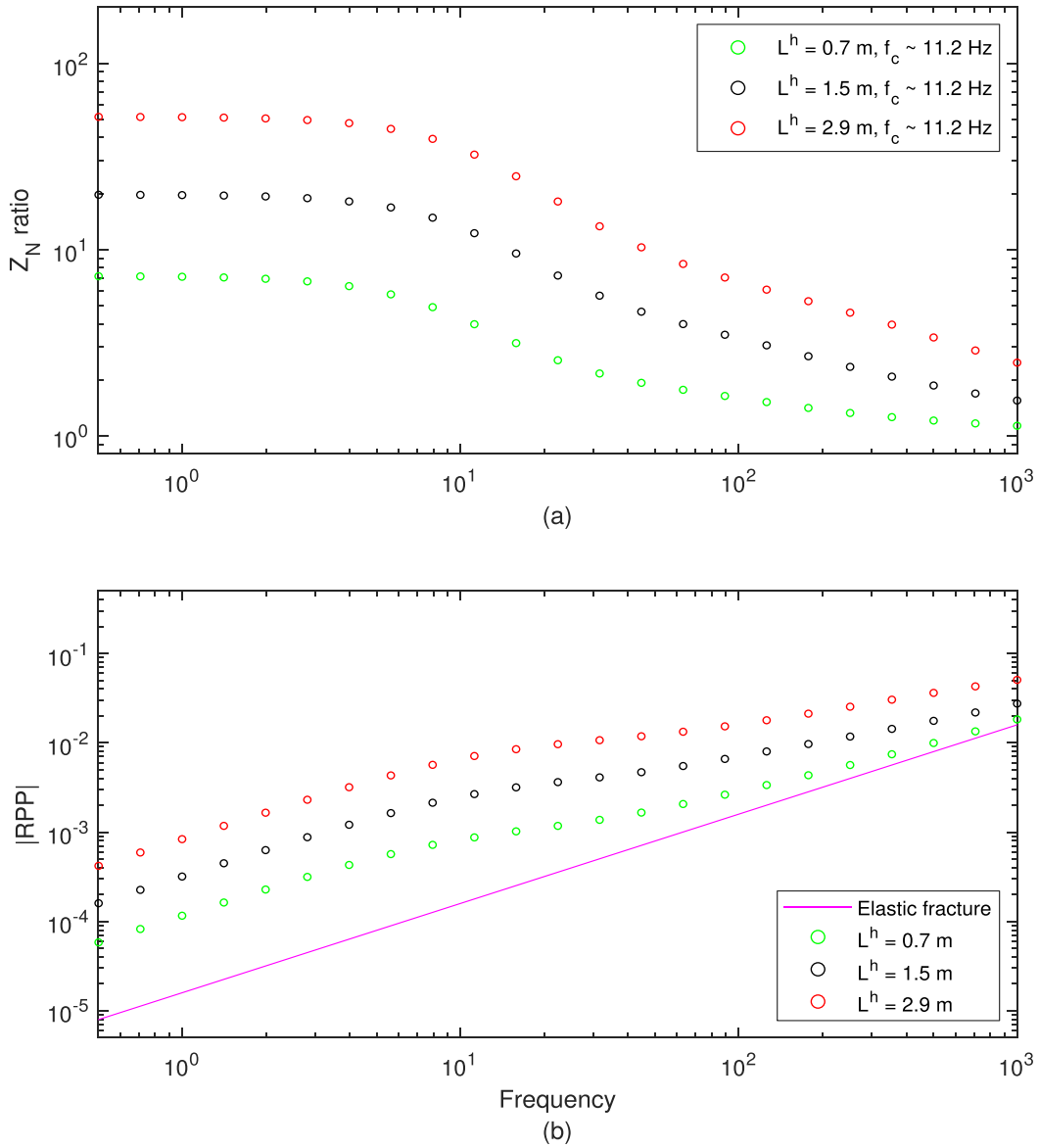

Figure 9. (a) Ratio of the primary fracture normal compliance to its undrained value (Z_N ratio) as a function of frequency considering secondary fractures presenting different properties correlated to their lengths L^h (Table 3). (b) Absolute value of the normal-incidence *P*-wave reflection coefficient as a function of frequency considering different frequency-dependent *P*-wave moduli of the primary fracture. These moduli include the FPD effects with secondary fractures having the same properties as in panel (a).

crust revealed their relation to both large- and small-scale fractures. An associated percolation analysis using seismic-derived fracture density pointed to the likely connectivity of these fractures. The results point to the existence of fracture zones with a high probability of interconnected pathways for fluid flow. Schreiter *et al.* (2015) estimated the reflection coefficients of imaged reflectors associated with fault zones. One of the highest reflectivities, as quantified by an average reflection coefficient of ~ -0.2 was interpreted as being due to the interaction of the seismic waves with a low-velocity region associated with a particular fault zone. In an independent analysis, Lüschen *et al.* (2015) suggested that the enhanced seismic attenuation found in some regions along this fault zone was an indication of a region of highly fractured and porous rock, which, in turn, would allow for enhanced energy dissipation due to FPD. These works provide evidence that secondary fractures associated with primary faults zones enhance their seismic visibility. Quite importantly, the available evidence also demonstrates that these fault-fracture systems tend to be characterized by a high degree of hydraulic interconnectivity.

4.2 Directions of future research

While there is strong evidence that FPD between large primary and smaller secondary fractures can contribute to the overall seismic visibility of the former, the quantitative analysis and interpretation of the underlying FPD effects remain to be resolved. In this regard, an interesting and important outcome of our work is that this problem could be addressed through finding an effective frequency-dependent *P*-wave modulus for the primary fracture, which incorporates the FPD effects of the secondary fractures. A

potential application would then be to estimate this modulus from reflected signals partitioned at several frequency bands to establish whether or not the modulus has a frequency-dependent character, which could be indicative of the presence of connected secondary fractures.

In this work, we have considered idealized models to represent a large primary fracture connected to smaller secondary fractures. Although, in actual geological settings, fracture zones surrounding primary faults generally present more complex patterns, the major advantage of this simplified modelling approach is that it allows for a rigorous analysis and an intuitive understanding of the governing physical processes associated with FPD effects that these smaller secondary fractures have on the seismic reflectivity of the larger primary fracture. Indeed, it is the inherent minimalistic nature and the associated simplicity of our model that allows for establishing first-order relationships of cause and effect, as it retains the essential physics of the prevailing poroealastic interactions. In this context, it is important to note that in order to effectively investigate the potential impact of FPD effects, the proposed models consider arrangements of primary and secondary fractures that maximize FPD effects: secondary fractures orthogonally intersecting the primary fracture and a *P*-wave impinging normally onto the latter. This readily allows us to evaluate the associated wave propagation characteristics and, thus, to relate the properties of the secondary fractures and the associated FPD effects to the seismic reflectivity and compliance of the primary fracture. Unravelling these fundamental relationships would not have been possible with more complex models. However, now that the underlying physics has been elucidated, future works should focus on more realistic scenarios and applications.

In our models we have considered equally spaced secondary fractures. Nonetheless, we would like to discuss the possible FPD effects of randomly spaced secondary fractures on the seismic properties of primary fractures. We present this scenario as an example of the kind of increasing complexity that our modelling approach could evaluate under certain sampling considerations. Specifically, we assume a random spacing of secondary fractures such that: First, the spacing is in the mesoscale. Second, there exists a typical sample, which contains an average number of secondary fractures per sample size that adequately represents the fracture density of the entire system. Third, the size of the typical sample is smaller than or equal to the prevailing Fresnel zone. These considerations permit to obtain a typical sample for the homogenization procedure, and to ensure that it is affected by an impinging wave in its totality. For comparison, we consider an equal sample size that contains the same number of equally spaced secondary fractures as the average of the randomly spaced case. Note that the average spacing of the randomly spaced secondary fractures is expected to be comparable to that of the equally spaced case since in both cases a similar number of fractures per sample size is considered. In the following, we comment on the possible impact that the randomly spaced secondary fractures could have on the properties (compliance and reflectivity) of the associated primary fracture due to FPD. For the low-frequency regime, we suggest that the effect on the compliance and reflectivity of the primary fracture is similar to the one produced by the equally spaced counterpart. This is because the number of secondary fractures in both cases are similar, which provides comparable pore volume availability for FPD. On the other hand, it is expected that some differences arise in the transitional regime because this regime is very sensitive to the particular disposition of heterogeneities, in this case the individual spacing of secondary fractures in the randomly spaced scenario. Finally, the effect on the high-frequency regime would be as expected based on our current work because, in this regime, the primary fracture can be regarded as hydraulically isolated, which, in turn, causes it to behave elastically.

In our study, we have only considered the case of a largely impermeable background. This type of background constrains the FPD effects to prevail exclusively between the primary and secondary fractures. However, if we were to consider a background deemed permeable for the frequencies of interest, then FPD effects associated with this background would also arise. In the following, we discuss the impact that these additional FPD effects would have on the primary fracture properties, as well as the associated challenges to account for these effects in a quantitative analysis. To this end, we refer to the work of Rubino *et al.* (2014) who compare FPD effects in media with intersecting and non-intersecting fractures embedded in permeable backgrounds. Although they perform their analysis in the mesoscale, and, thus, consider an effective response of the fractured media, we believe that their results provide valuable insights to address this question. Rubino *et al.* (2014) demonstrate that considering intersecting fractures embedded in a permeable background involves two different types of FPD interactions: fracture-to-fracture and fracture-to-background. They also show that this, in turn, affects the frequency-dependent behaviour of the effective *P*-wave velocity with respect to the case of non-intersecting fractures. Likewise, we should also expect these two types of FPD interactions in our models in the presence of a permeable background: primary-to-secondary fractures and fractures-to-background. In this case, the term fractures refers to both primary and secondary. We therefore argue that the work of Rubino *et al.* (2014) suggests that adding a permeable background will modify the frequency-dependent behaviour of the the primary fracture properties to reflect both of these FPD interactions. However, a corresponding quantitative analysis with a homogenization method is still an unresolved problem since the challenge is to find boundary conditions that allow us to represent the effects of an infinite background in the considered sample. An alternative would be to perform numerical simulations of poroelasitc wave propagation.

Another important subject for future research is to test experimentally the numerical results presented in this study with respect to the normal compliance and reflectivity of primary large fractures due to the poroelastic effects induced by connected secondary fractures. As stated in the introduction, related experimental works, which explore poroelastic effects between fractures and their embedding porous background, show that the normal compliance of fractures has a frequency-dependent-behaviour due to the aforementioned poroelastic interactions and that models considering these effects explain better the available experimental data than solutions that disregard the poroelastic interactions.

5 CONCLUSIONS

We have investigated FPD effects between a water-saturated large primary fracture and perpendicular intersecting smaller mesoscale secondary fractures induced by a *P*-wave impinging normally onto the primary fracture. We have performed a sensitivity analysis of the compliance and of the normal-incidence PP reflectivity of the primary fracture with regard to variations of different geometrical and physical properties of the secondary fractures.

Our results show that FPD interactions between the primary and secondary fractures in the relaxed and transitional regimes produce

an increase of the normal compliance and normal-incidence PP reflectivity of the primary fracture with respect to the case that disregards the secondary fractures, in which the primary fracture behaves as an elastic medium. However, secondary fractures with different sets of physical and geometrical properties affect the magnitude of the relaxed normal compliance of the primary fracture in varying ways. For instance, gas-saturated secondary fractures induce the highest increase, ∼150-folds, of the relaxed normal compliance. This, in turn, produces a maximum increase of the reflectivity of the primary fracture of ∼1.5-orders-of-magnitude. On the other hand, results of the sensitivity analyses show that it is the variations of the length of the secondary fractures that have the largest impact on changes of the relaxed normal compliance of the primary fracture.

Our results also show that the characteristic transition frequency f_c associated with the normal compliance of the primary fracture controls the seismic visibility of the reflectivity of the primary fracture since it determines the frequency shift from the relaxed toward the unrelaxed FPD regime. The value of fc is, in turn, influenced either in a direct or inverse manner by the fractional volume of the secondary fractures, their geometrical and physical properties as well as the viscosity of their saturating fluid. Overall, the results of our study suggest that mesoscopic secondary fractures connected to a large primary fracture can induce FPD effects that substantially enhance the seismic visibility of the primary fracture.

In this study, we have considered an idealized but instructive canonical model of secondary fractures, which has allowed us to investigate the impact that the associated FPD has on the normal compliance and the PP reflectivity of a primary fracture connected to secondary ones. To deepen our understanding of the influence of mesoscopic secondary fractures on the seismic behaviour of macroscale primary fractures due to FPD effects, it will be essential to explore more realistic scenarios of secondary fractures networks. Another important extension of the current work will be the evaluation of the reflectivity of such fracture systems for non-normal angles of incidence.

FUNDING

This work was funded by the Swiss National Science Foundation: grant # 200020-178946, CONICET: grant # PIP 11220210100346CO and the Horizon 2020 Programme of the European Commission: grant number # 101007851.

ACKNOWLEDGMENTS

This work was supported by grant # 200020-178946 from the Swiss National Science Foundation. JGR gratefully acknowledges the financial support received from CONICET (PIP 11220210100346CO). We acknowledge the financial support of the European Commission through the DISCO2 STORE project with grant agreement ID 101007851 of the Horizon 2020 Programme.

AUTHOR CONTRIBUTIONS

Edith Sotelo (Formal analysis, Investigation, Methodology, Writing—original draft, Writing—review & editing), J. Germán Rubino (Conceptualization, Formal analysis, Investigation, Methodology, Supervision, Writing—original draft, Writing—review & editing), Nicolás D. Barbosa (Formal analysis, Investigation, Writing—original draft, Writing—review & editing), Santiago G. Solazzi (Conceptualization, Methodology, Writing—original draft, Writing—review & editing) and Klaus Holliger (Conceptualization, Investigation, Project administration, Resources, Writing—original draft, Writing—review & editing).

DATA AVAILABILITY

The code used to generate the data for this study is available at the Zenodo repository via https://doi.org/10.5281/zenodo.11062294 (doi:10.5281/zenodo.11062294) with Creative Commons Attribution 4.0 International Public License (Favino 2024).

The scripts to run the code and the corresponding results used to create the figures of this study are available at the Zenodo repository via https://doi.org/10.5281/zenodo.10933613 (doi:10.5281/zenodo.10933613) with Creative Commons Attribution 4.0 International Public License (Sotelo *et al.* 2024).

REFERENCES

Adam, E., Perron, G., Milkereit, B., Wu, J., Calvert, A.J., Salisbury, M., Verpaelst, P. & Dion, D.-J., 2000. A review of high-resolution seismic profiling across the Sudbury, Selbaie, Noranda, and Matagami mining camps1, *Can. J. Earth Sci.,* **37**(2–3), 503–516.

Ahmed, K.A., Schwarz, B. & Gajewski, D., 2015. Application of the 3D common-reflection-surface stack workflow in a crystalline rock environment, *Geophys. Prospect.,* **63**(4), 990–998.

Barbosa, N.D., Rubino, J.G., Caspari, E., Milani, M. & Holliger, K., 2016. Fluid pressure diffusion effects on the seismic reflectivity of a single fracture, *J. acoust. Soc. Am.,* **140**(4), 2554–2570.

Barbosa, N.D., Rubino, J.G., Caspari, E. & Holliger, K., 2017. Extension of the classical linear slip model for fluid-saturated fractures: Accounting for fluid pressure diffusion effects, *J. Geophys. Res. Solid Earth,* **122**(2), 1302–1323.

Barbosa, N.D., Caspari, E., Rubino, J.G., Greenwood, A., Baron, L. & Holliger, K., 2019. Estimation of fracture compliance from attenuation and velocity analysis of full-waveform sonic log data, *J. Geophys. Res. Solid Earth,* **124**(3), 2738–2761.

Bergman, B., Juhlin, C. & Palm, H., 2002. High-resolution reflection seismic imaging of the upper crust at Laxemar, southeastern Sweden, *Tectonophysics,* **355**(1), 201–213.

Biot, M.A., 1956. Theory of propagation of elastic waves in a fluid-saturated porous solid. II. Higher frequency range, *J. acoust. Soc. Am.,* **28**(2), 179–191.

Biot, M.A., 1962. Mechanics of deformation and acoustic propagation in porous media, *J. Appl. Phys.,* **33**(4), 1482–1498.

Bonnet, E., Bour, O., Odling, N.E., Davy, P., Main, I., Cowie, P. & Berkowitz, B., 2001. Scaling of fracture systems in geological media, *Rev. Geophys.,* **39**(3), 347–383.

Bruhn, R.L., Parry, W.T., Yonkee, W.A. & Thompson, T., 1994. Fracturing and hydrothermal alteration in normal fault zones, *Pure appl. Geophys.,* **142**(3), 609–644.

Casini, M., Ciuffi, S., Fiordelisi, A., Mazzotti, A. & Stucchi, E., 2010. Results of a 3-D seismic survey at the Travale (Italy) test site, *Geothermics,* **39**(1), 4–12.

Chandler, R.N. & Johnson, D.L., 1981. The equivalence of quasistatic flow in fluid-saturated porous media and Biot's slow wave in the limit of zero frequency, *J. Appl. Phys.,* **52**(5), 3391–3395.

Chapman, M., 2003. Frequency-dependent anisotropy due to meso-scale fractures in the presence of equant porosity, *Geophys. Prospect.,* **51**(5), 369–379.

Cheraghi, S., Malehmir, A., Naghizadeh, M., Snyder, D., Mathieu, L. & Bedeaux, P., 2021. Seismic imaging across fault systems in the Abitibi greenstone belt–an analysis of pre- and post-stack migration approaches in the Chibougamau area, Quebec, Canada, *Solid Earth,* **12**(5), 1143–1164.

Chester, F.M., Chester, J.S., Kirschner, D.L., Schulz, S.E. & Evans, J.P., 2004. Structure of large-displacement, strike-slip fault zones in the brittle continental crust, in *Rheology and Deformation of the Lithosphere at Continental Margins,* pp. 223–260, eds Karner, G.D., Taylor, B., Driscoll, N.W. & Kohlstedt, D.L., Columbia University Press, New York.

Cui, X., Krebes, E.S. & Lines, L.R., 2017. Seismic inversion for geologic fractures and fractured media, *Geophysics,* **82**(5), C145–C161.

De Dreuzy, J.R., Davy, P. & Bour, O., 2001. Hydraulic properties of two-dimensional random fracture networks following a power law length distribution: 2. Permeability of networks based on lognormal distribution of apertures, *Water Resour. Res.,* **37**(8), 2079–2095.

Dutta, N.C. & Odé, H., 1979. Attenuation and dispersion of compressional waves in fluid-filled porous rocks with partial gas saturation (White model)—Part I: Biot theory, *Geophysics,* **44**(11), 1777–1788.

Fang, X., Fehler, M., Chen, T., Burns, D. & Zhu, Z., 2013. Sensitivity analysis of fracture scattering, *Geophysics,* **78**(1), T1–T10.

Faulkner, D., Jackson, C., Lunn, R., Schlische, R., Shipton, Z., Wibberley, C. & Withjack, M., 2010. A review of recent developments concerning the structure, mechanics and fluid flow properties of fault zones, *J. Struct. Geol.,* **32**(11), 1557–1575.

Favino, M., 2024. [Software]. favinom/parrotc:parrotc202404, Zenodo.

Favino, M., Hunziker, J., Caspari, E., Quintal, B., Holliger, K. & Krause, R., 2020. Fully-automated adaptive mesh refinement for media embedding complex heterogeneities: application to poroelastic fluid pressure diffusion, *Comput. Geosci.,* **24**(3), 1101–1120.

Glaas, C., Vidal, J. & Genter, A., 2021. Structural characterization of naturally fractured geothermal reservoirs in the central Upper Rhine Graben, *J. Struct. Geol.,* **148,** 104 370, doi:10.1016/j.jsg.2021.104370.

Gu, B., Suárez-Rivera, R., Nihei, K.T. & Myer, L.R., 1996. Incidence of plane waves upon a fracture, *J. Geophys. Res. Solid Earth,* **101**(B11), 25 337–25 346.

Gudmundsson, A., Berg, S.S., Lyslo, K.B. & Skurtveit, E., 2001. Fracture networks and fluid transport in active fault zones, *J. Struct. Geol.,* **23**(2–3), 343–353.

Guo, J., Rubino, J.G., Glubokovskikh, S. & Gurevich, B., 2017. Effects of fracture intersections on seismic dispersion: theoretical predictions versus numerical simulations, *Geophys. Prospect.,* **65**(5), 1264–1276.

Harjes, H.-P. *et al.*, 1997. Origin and nature of crystal reflections: results from integrated seismic measurements at the KTB superdeep drilling site, *J. Geophys. Res. Solid Earth,* **102**(B8), 18 267–18 288.

Hatton, C.G., Main, I.G. & Meredith, P.G., 1994. Non-universal scaling of fracture length and opening displacement, *Nature,* **367**(6459), 160–162.

Hobday, C. & Worthington, M.H., 2012. Field measurements of normal and shear fracture compliance, *Geophys. Prospect.,* **60**(3), 488–499.

Hunziker, J., Favino, M., Caspari, E., Quintal, B., Rubino, J.G., Krause, R. & Holliger, K., 2018. Seismic attenuation and stiffness modulus dispersion in porous rocks containing stochastic fracture networks, *J. Geophys. Res. Solid Earth,* **123**(1), 125–143.

Hyman, J.D., Aldrich, G., Viswanathan, H., Makedonska, N. & Karra, S., 2016. Fracture size and transmissivity correlations: implications for transport simulations in sparse three-dimensional discrete fracture networks following a truncated power law distribution of fracture size, *Water Resour. Res.,* **52**(8), 6472–6489.

Jaeger, J.C., Cook, N.G.W. & Zimmerman, R., 2007. Hydromechanical behaviour of fractures, in *Fundamentals of Rock Mechanics,* 4th edn. Wiley.

Kim, Y.S., Peacock, D.C. & Sanderson, D.J., 2004. Fault damage zones, *J. Struct. Geol.,* **26**(3), 503–517.

Liu, E., 2005. Effects of fracture aperture and roughness on hydraulic and mechanical properties of rocks: implication of seismic characterization of fractured reservoirs, *J. Geophys. Eng.,* **2**(1), 38–47.

Liu, E., Hudson, J.A., Crampin, S., Rizer, W.D., Queen, J.H. & Rossmanith, H.P., 1995. Seismic properties of a general fracture, in *Mechanics of Jointed and Faulted Rock,* pp. 673–678.CRC Press

Lubbe, R. & Worthington, M.H., 2006. A field investigation of fracture compliance, *Geophys. Prospect.,* **54**(3), 319–331.

Lüschen, E., Görne, S., von Hartmann, H., Thomas, R. & Schulz, R., 2015. 3D seismic survey for geothermal exploration in crystalline rocks in Saxony, Germany, *Geophys. Prospect.,* **63**(4), 975–989.

Minato, S. & Ghose, R., 2014. Imaging and characterization of a subhorizontal non-welded interface from point source elastic scattering response, *Geophys. J. Int.,* **197**(2), 1090–1095.

Minato, S. & Ghose, R., 2016. AVO inversion for a non-welded interface: estimating compliances of a fluid-filled fracture, *Geophys. J. Int.,* **206**(1), 56–62.

Mitchell, T.M. & Faulkner, D.R., 2009. The nature and origin of off-fault damage surrounding strike-slip fault zones with a wide range of displacements: a field study from the Atacama fault system, northern Chile, *J. Struct. Geol.,* **31**(8), 802–816.

Mitchell, T.M. & Faulkner, D.R., 2012. Towards quantifying the matrix permeability of fault damage zones in low porosity rocks, *Earth planet. Sci. Lett.,* **339–340,** 24–31.

Morris, J.P., Jocker, J. & Prioul, R., 2017. Numerical investigation of alternative fracture stiffness measures and their respective scaling behaviours, *Geophys. Prospect.,* **65**(3), 791–807.

Müller, T.M., Gurevich, B. & Lebedev, M., 2010. Seismic wave attenuation and dispersion resulting from wave-induced flow in porous rocks—a review, *Geophysics,* **75**(5), 75A147–75A164.

Nakagawa, S., 2013. Low-frequency (\textless 100 Hz) dynamic fracture compliance measurement in the laboratory, in *47th Rock Mechanics, Geomechanics Symposium,* American Rock Mechanics Association, San Fracisco.

Nakagawa, S. & Schoenberg, M.A., 2007. Poroelastic modelling of seismic boundary conditions across a fracture, *J. acoust. Soc. Am.,* **122**(2), 831–847.

Norris, A.N., 1993. Low-frequency dispersion and attenuation in partially saturated rocks, *J. acoust. Soc. Am.,* **94**(1), 359–370.

Pride, S.R., Berryman, J.G. & Harris, J.M., 2004. Seismic attenuation due to wave-induced flow, *J. Geophys. Res. Solid Earth,* **109**(B1), doi:10.1029/2003JB002639.

Pyrak-Nolte, L.J., Myer, L.R. & Cook, N.G.W., 1990. Transmission of seismic waves across single natural fractures, *J. geophys. Res.,* **95**(B6), 8617, doi:10.1029/JB095iB06p08617.

Quintal, B., Steeb, H., Frehner, M. & Schmalholz, S.M., 2011. Quasi-static finite element modelling of seismic attenuation and dispersion due to wave-induced fluid flow in poroelastic media, *J. Geophys. Res. Solid Earth,* **116**(B1), doi:10.1029/2010JB007475.

Quintal, B., Jänicke, R., Rubino, J.G., Steeb, H. & Holliger, K., 2014. Sensitivity of *S*-wave attenuation to the connectivity of fractures in fluid-saturated rocks, *Geophysics,* **79**(5), WB15–WB24.

Renshaw, C.E., 1995. On the relationship between mechanical and hydraulic apertures in rough-walled fractures, *J. geophys. Res.,* **100**(B12), 24 629–24 636.

Rubino, J.G., Ravazzoli, C.L. & Santos, J.E., 2009. Equivalent viscoelastic solids for heterogeneous fluid-saturated porous rocks, *Geophysics,* **74**(1), N1–N13.

Rubino, J.G., Guarracino, L., Müller, T.M. & Holliger, K., 2013. Do seismic waves sense fracture connectivity?, *Geophys. Res. Lett.,* **40**(4), 692–696.

Rubino, J.G., Müller, T.M., Guarracino, L., Milani, M. & Holliger, K., 2014. Seismoacoustic signatures of fracture connectivity, *J. Geophys. Res. Solid Earth,* **119**(3), 2252–2271.

Rubino, J.G., Castromán, G.A., Müller, T.M., Monachesi, L.B., Zyserman, F.I. & Holliger, K., 2015. Including poroelastic effects in the linear slip theory, *Geophysics,* **80**(2), A51–A56.

Rubino, J.G., Caspari, E., Müller, T.M., Milani, M., Barbosa, N.D. & Holliger, K., 2016. Numerical upscaling in 2-D heterogeneous poroelastic rocks: anisotropic attenuation and dispersion of seismic waves, *J. Geophys. Res. Solid Earth,* **121**(9), 6698–6721.

Sausse, J. & Genter, A., 2005. Types of permeable fractures in granite, *Geol. Soc. Spec. Publ.,* **240,** 1–14.

Savage, H.M. & Brodsky, E.E., 2011. Collateral damage: evolution with displacement of fracture distribution and secondary fault strands in fault damage zones, *J. Geophys. Res. Solid Earth,* **116**(3), doi:10.1002/2014JB011652.

Schoenberg, M., 1980. Elastic wave behaviour across linear slip interfaces, *J. acoust. Soc. Am.,* **68**(5), 1516–1521.
Schreiter, L., Hloušek, F., Hellwig, O. & Buske, S., 2015. Characterization of seismic reflections from faults in a crystalline environment, Schneeberg, Germany, *Geophys. Prospect.,* **63**(4), 1015–1032.
Solazzi, S.G., Hunziker, J., Caspari, E., Rubino, J.G., Favino, M. & Holliger, K., 2020. Seismic signatures of fractured porous rocks: the partially saturated case, *J. Geophys. Res.: Solid Earth,* **125**(8), doi:10.1029/2020JB019960.
Song, Y., Rudnicki, J.W., Hu, H. & Han, B., 2020. Dynamics anisotropy in a porous solid with aligned slit fractures, *J. Mech. Phys. Solids,* **137,** 1–22.
Sotelo, E., Rubino, J.G., Solazzi, S.G., Barbosa, N.D. & Holliger, K., 2021. Fractures in low-permeability rocks: can poroelastic effects associated with damage zones enhance their seismic visibility?, *J. Geophys. Res. Solid Earth,* **126**(5), e2020JB021155, doi:10.1029/2020JB021155.
Sotelo, E., Barbosa, N.D., Solazzi, S.G., Rubino, J.G., Favino, M. & Holliger, K., 2023. Homogenization of porous thin layers with internal stratification for the estimation of seismic reflection coefficients, *J. Geophys. Res. Solid Earth,* **128**(11), e2023JB026782, doi:10.1029/2023JB026782.
Sotelo, E., Rubino, J.G., Barbosa, N.D. & Solazzi, S.G., 2024. [Dataset]. Impact of connected secondary fractures on the seismic reflectivity of large primary fractures, Zenodo.
Szalaiová, E., Iwanowski-Strahser, K. & Rabbel, W., 2015. 3-D fracture networks in the crystalline upper crust—a new seismic model of the Continental Deep Drilling Site (South Germany), *Geophys. Prospect.,* **63**(4), 937–956.
Tsang, C.-F. & Neretnieks, I., 1998. Flow channeling in heterogeneous fractured rocks, *Rev. Geophys.,* **36**(2), 275–298.
Verdon, J.P. & Wüstefeld, A., 2013. Measurement of the normal/tangential fracture compliance ratio (ZN/ZT) during hydraulic fracture stimulation using S-wave splitting data, *Geophys. Prospect.,* **61**(s1), 461–475.
Vidal, J., Genter, A. & Chopin, F., 2017. Permeable fracture zones in the hard rocks of the geothermal reservoir at Rittershoffen, France, *J. Geophys. Res. Solid Earth,* **122**(7), 4864–4887.
Wang, D., Qu, S.L., Ding, P.B. & Zhao, Q., 2017. Analysis of dynamic fracture compliance based on poroelastic theory. Part I: model formulation and analytical expressions, *Pure appl. Geophys.,* **174**(5), 2103–2120.
Wang, D., bo Ding, P. & Ba, J., 2018. Analysis of dynamic fracture compliance based on poroelastic theory. Part II: results of numerical and experimental tests, *Pure appl. Geophys.,* **175**(8), 2987–3001.
Wenzlau, F., Altmann, J.B. & Müller, T.M., 2010. Anisotropic dispersion and attenuation due to wave-induced fluid flow: quasi-static finite element modelling in poroelastic solids, *J. geophys. Res.,* **115**(B7), 7204, doi:10.1029/2009JB006644.
Worthington, M.H. & Lubbe, R., 2007. The scaling of fracture compliance, *Geol. Soc. Spec. Publ.,* **270**(1), 73–82.
Zhou, Z., Caspari, E., Barbosa, N.D., Greenwood, A. & Holliger, K., 2022. Mechanical compliance of individual fractures in a heterogeneous rock mass from production-type full-waveform sonic data, *J. Geophys. Res. Solid Earth,* **127**(8), e2022JB024302, doi:10.1029/2022JB024302.
Zimmerman, R.W. & Bodvarsson, G.S., 1996. Hydraulic conductivity of rock fractures, *Transport in Porous Media,* **23**(1), 1–30.

APPENDIX A: MESOSCALE FPD AND ITS ASSOCIATED PRESSURE RELAXATION MECHANISM

Mesoscale FPD prevails between heterogeneities presenting characteristic length scales l_h much larger than the pore scale l_p but much smaller than the wavelength λ_w. For the considered fracture system (Fig. 1), the mesoscale heterogeneities are governed by the characteristic sizes of the secondary fractures, for instance, their length or aperture (Rubino *et al.* 2014). FPD describes a flow mechanism where viscous drag between the rock frame and the pore fluid dominates. This mechanism prevails at sufficiently low frequencies. As frequencies increase, the drag becomes increasingly influenced by inertia, limiting the applicability of FPD for describing wave-induced fluid flow. The transition frequency between these two regimes is known as Biot's characteristic frequency f_B. Therefore, FPD is valid only for frequencies f that are much lower than Biot's characteristic frequency f_B, which can be defined as (e.g. Biot 1956; Dutta & Odé 1979)

$$f_B = \frac{1}{2\pi}\frac{\eta\phi}{\rho_f \kappa S}, \tag{A1}$$

where ϕ is the porosity, κ the static permeability, η the fluid viscosity, ρ_f the fluid density and S the tortuosity of the pore space. The aforementioned considerations regarding frequencies and scales constraining mesoscale FPD can be summarized as

$$\begin{aligned} &f \ll f_B, \\ &l_p \ll l_h \ll \lambda_w. \end{aligned} \tag{A2}$$

Studies have shown that a diffusion equation governing FPD can be obtained from Biot's 1962 quasi-static poroelasticity equations. Alternatively, it can be derived from the corresponding dynamic equations by neglecting inertial terms (Dutta & Odé 1979; Chandler & Johnson 1981). This diffusion equation is linked to the slow, diffusive *P*-wave (Dutta & Odé 1979) and it is associated to a frequency-dependent diffusion length L_d given by (Norris 1993)

$$L_d = \sqrt{\frac{D}{\omega}}, \tag{A3}$$

where ω is the angular frequency, with $\omega = 2\pi f$, and D is the diffusion coefficient.

Guo *et al.* (2017) suggest the following expression for the diffusion coefficient D for a fractured medium consisting of mutually orthogonal fracture sets embedded in a background deemed impermeable for the frequencies of interest

$$D = \frac{M^m H_d^m}{H_s^m}\left(\frac{\beta\,\kappa^{fr}}{\eta}\right), \tag{A4}$$

where M^m is the Biot's storage fluid modulus, H_d^m and H_s^m are the drained and the low-frequency *P*-wave moduli, respectively. Here, the superscript m refers to the effective properties of the fractured medium and the term low-frequency refers to the frequency range in which the relaxed pressure regime prevails. This implies that there is enough time for the pressure to equilibrate as fluid flows between the primary and secondary fractures. Next, β is the fractional volume occupied by the fractures and κ^{fr} is the permeability of the fractures. Eq. (A4) assumes that the fractured medium is represented by an effective one and that the size of the fractures are in the mesoscopic scale range. However, these assumptions do no longer apply to the model under study, which considers an infinite horizontal primary fracture intersected by mesoscale secondary ones embedded in a full-space background (Fig. 1). Nevertheless, eq. (A4) can be used as a reference since the FPD process is very similar in both fracture systems. For the medium with intersecting orthogonal mesoscale fractures, a *P*-wave impinging normally onto one of the fracture sets creates a fluid pressure increase inside their pores that equilibrates as the fluid flows into the intersecting fractures. We argue that this FPD process is comparable to the one prevailing in our model, in that a *P*-wave impinging normally onto the large primary fracture increases, in a similar way, the pressure inside this fracture, which, in turn, also induces fluid flow onto the orthogonally

intersecting secondary ones as pressure equilibrates. If we additionally assume that the properties of the background and the primary fracture remain invariant, then, according to eq. (A4), variations in the diffusion coefficient D depend solely on the properties of the secondary fractures.

FPD exhibits two distinct regimes, the relaxed and the unrelaxed states, which are governed by the frequency-dependent diffusion length L_{d} and the characteristic size of the heterogeneities l_{h}. The relaxed regime dominates at sufficiently low frequencies where L_{d} is much larger than l_{h}. In this regime, there is ample time for pressure between the primary and secondary fractures to equalize. The unrelaxed regime prevails at sufficiently high frequencies where L_{d} is significantly smaller than l_{h}. Consequently, there is not enough time for pressure to equilibrate, and, as a result, the fractures become hydraulically isolated. A transition zone exists between these regimes at intermediate frequencies, for which L_{d} approaches l_{h}. This zone is characterized by a critical transition frequency, denoted by $f_{\mathrm{c}} = \omega_{\mathrm{c}}/2\pi$, which is determined by the diffusion coefficient D and the size of the heterogeneities l_{h} (Guo *et al.* 2017)

$$\omega_{\mathrm{c}} = \frac{2D}{(l_{\mathrm{h}})^2}. \tag{A5}$$

APPENDIX B: POROELASTIC-TO-VISCOELASTIC HOMOGENIZATION PROCEDURE

B1 Mathematical model

In the following, we detail the homogenization procedure of the considered fracture system (Fig. 1), which consists of an infinite horizontal primary fracture intersected by secondary vertical ones embedded in a background deemed impermeable for the frequencies of interest.

First, we present the governing equations used in the homogenization procedure. These are Biot's quasi-static equations (Biot 1962), which we solve over the sample Ω (Fig. 2) for the vertical compressional oscillatory relaxation test. We express these equations in the solid displacement–pressure ($\boldsymbol{u} - p$) formulation in the frequency domain (e.g. Quintal *et al.* 2011; Favino *et al.* 2020), with $\boldsymbol{u} = \boldsymbol{u}(\boldsymbol{x}, \omega)$ and $p = p(\boldsymbol{x}, \omega)$, where $\boldsymbol{x} \in \Omega$ is the position and $\omega \in F$ is the angular frequency, with $F = (0, W]$. This yields

$$\begin{aligned} &-\nabla \cdot \boldsymbol{\sigma} = \boldsymbol{0} \quad \text{in} \quad \Omega \times F, \\ &-i\,\alpha \nabla . \boldsymbol{u} - i\,\frac{p}{M} + \frac{1}{\omega}\,\nabla \cdot \left(\frac{\kappa}{\eta}\nabla p\right) = 0 \quad \text{in} \quad \Omega \times F, \end{aligned} \tag{B1}$$

where $\boldsymbol{\sigma}$ is the total stress and i is the imaginary unit, α is the Biot–Willis effective stress coefficient, M is Biot's fluid storage modulus, κ is the permeability and the term $(\frac{\kappa}{\eta}\nabla p)$ denotes the Darcy flux.

The constitutive equation relating the total stress $\boldsymbol{\sigma}$ to $\boldsymbol{u}$ and p is

$$\begin{aligned} &\boldsymbol{\sigma} = 2\mu\,\boldsymbol{\varepsilon} + (\lambda_{\mathrm{d}}\ \mathrm{tr}(\boldsymbol{\varepsilon})\ - \alpha\ p)\,\boldsymbol{I}, \qquad \text{with} \\ &\boldsymbol{\varepsilon} = \frac{1}{2}\left(\nabla \boldsymbol{u} + (\nabla \boldsymbol{u})^T\right), \end{aligned} \tag{B2}$$

where $\boldsymbol{\varepsilon}$ is the strain tensor, $\boldsymbol{I}$ the identity tensor, μ is the shear modulus and λ_{d} is the drained Lamé modulus.

The required rock physical properties are calculated as

$$\begin{aligned} \lambda_{\mathrm{d}} &= K_{\mathrm{m}} - \frac{2}{3}\mu, \\ \alpha &= 1 - \frac{K_{\mathrm{m}}}{K_{\mathrm{s}}}, \\ M &= \left(\frac{\alpha - \phi}{K_{\mathrm{s}}} + \frac{\phi}{K_{\mathrm{f}}}\right)^{-1}, \end{aligned} \tag{B3}$$

where K_{m}, K_{s} and K_{f} are the bulk moduli of the drained solid frame, the solid grains and the pore fluid, respectively.

Next, we describe the vertical compressional oscillatory test applied as a BC in order to solve the governing equations. To this end, we consider a Cartesian coordinate system in 2-D space $\mathbb{R}^2$. The associated basis vectors $\hat{\boldsymbol{x}}_{\boldsymbol{1}}$ and $\hat{\boldsymbol{x}}_{\boldsymbol{3}}$ are aligned with the horizontal and vertical Cartesian axes, respectively. We also let the sample Ω be a quadrilateral. The boundary of this domain, denoted by Γ, is comprised by four segments: Γ_1^+, Γ_1^-, Γ_3^+ and Γ_3^-. Segments Γ_1^+ and Γ_1^- are opposite sides with outer normal vectors $\hat{\boldsymbol{x}}_{\boldsymbol{1}}$ and $-\hat{\boldsymbol{x}}_{\boldsymbol{1}}$, respectively. Likewise, segments Γ_3^+ and Γ_3^- are opposite sides with outer normal vectors $\hat{\boldsymbol{x}}_{\boldsymbol{3}}$ and $-\hat{\boldsymbol{x}}_{\boldsymbol{3}}$, respectively (Fig. 2). For notational simplicity, we define $\hat{\boldsymbol{n}}$ as the outward normal vector of Γ.

In the following, we define the BC for displacements $\boldsymbol{u}$, pressure p, tractions $\boldsymbol{\sigma} \cdot \hat{\boldsymbol{n}}$ and the component normal to the boundary of the Darcy flux $(\frac{\kappa}{\eta}\nabla p \cdot \hat{\boldsymbol{n}})$. We impose periodicity for the respective variables on opposing boundaries of the sample as follows

The BC for displacements are

$$\begin{aligned} &\boldsymbol{u} \cdot \hat{\boldsymbol{x}}_{\boldsymbol{3}}\,|_{\Gamma_3^-} - \boldsymbol{u} \cdot \hat{\boldsymbol{x}}_{\boldsymbol{3}}\,|_{\Gamma_3^+} = -\Delta u, \\ &\boldsymbol{u} \cdot \hat{\boldsymbol{x}}_{\boldsymbol{1}}\,|_{\Gamma_3^-} - \boldsymbol{u} \cdot \hat{\boldsymbol{x}}_{\boldsymbol{1}}\,|_{\Gamma_3^+} = 0, \\ &\boldsymbol{u}\,|_{\Gamma_1^+} - \boldsymbol{u}\,|_{\Gamma_1^-} = \boldsymbol{0}, \end{aligned} \tag{B4}$$

where Δu is a real displacement difference in the frequency domain. The first line of eq. (B4) sets the BC corresponding to the vertical compressional oscillatory test.

The respective BC for pressure, tractions and the Darcy flux are

$$\begin{aligned} &p|_{\Gamma_k^+} - p|_{\Gamma_k^-} = 0, \\ &(\boldsymbol{\sigma} \cdot \hat{\boldsymbol{n}})\,|_{\Gamma_k^+} - (\boldsymbol{\sigma} \cdot \hat{\boldsymbol{n}})\,|_{\Gamma_k^-} = \boldsymbol{0}, \\ &\left(\frac{\kappa}{\eta}\nabla p \cdot \hat{\boldsymbol{n}}\right)|_{\Gamma_k^+} - \left(\frac{\kappa}{\eta}\nabla p \cdot \hat{\boldsymbol{n}}\right)|_{\Gamma_k^-} = 0, \end{aligned} \tag{B5}$$

where the subscript k in Γ_k^- and Γ_k^+ takes the value of 1 or 3 to denote opposite boundaries.

Finally, we present the derivation of the P-wave modulus and normal compliance of the primary fracture. We first obtain the average of the stress component $\langle \sigma_{33} \rangle_{\Omega_{p1}}$ and that of the strain component $\langle \varepsilon_{33} \rangle_{\Omega_{p1}}$ over the subdomain Ω_{p1}, which is the one corresponding to the primary fracture (Fig. 2). The calculation of the average quantities $\langle \square \rangle_{\Omega_{p1}}$ are performed as follows

$$\langle \square \rangle_{\Omega_{p1}} = \frac{1}{|\Omega_{p1}|}\int_{\Omega_{p1}} \square\, d\Omega_{p1}, \quad \text{with} \quad |\Omega_{p1}| = \int_{\Omega_{p1}} d\Omega_{p1}. \tag{B6}$$

Then, we compute the complex-valued and frequency-dependent P-wave modulus $H(\omega)$ of the primary fracture as

$$H(\omega) = \frac{\langle \sigma_{33} \rangle_{\Omega_{p1}}}{\langle \varepsilon_{33} \rangle_{\Omega_{p1}}}. \tag{B7}$$

Next, we obtain the complex-valued and frequency-dependent normal compliance $Z_{\mathrm{N}}(\omega)$ of the primary fracture as

$$Z_{\mathrm{N}}(\omega) = \frac{a^f}{H(\omega)}, \tag{B8}$$

where a^f is the aperture of the primary fracture.

We remark that the transition frequency f_c can be evaluated as the frequency associated with the maximum magnitude of the imaginary part of the normal compliance ($|\,\mathrm{Im}(Z_N(\omega))|$) (Rubino *et al.* 2015).

B2 Finite element solution

In the following, we present the finite element solution of Biot's (1956,1962) governing eq. (B1). The procedure is the one proposed by Favino *et al.* (2020), who developed a computationally cost-effective adaptive meshing approach to discretize domains with complex heterogeneities. This technique creates non-conforming meshes and local refinements through automatic adaptions of an initial uniform mesh.

First, we present the weak formulation of Biot's (1956, 1962) eq. (B1). We refer the reader to Favino *et al.* (2020) for the details of the mathematical treatment. We consider a complex-valued vector function $\boldsymbol{v}$, with complex conjugate $\boldsymbol{v}^*$, which multiplies the first line of eq. (B1). We also consider a scalar function q in the complex domain, with complex conjugate q^*, which multiplies the second line of eq. (B1). The corresponding inner products are

$$\begin{aligned}&\int_\Omega (\nabla\cdot\boldsymbol{\sigma})\cdot\boldsymbol{v}^*\,\mathrm{d}\Omega = 0,\\ &-i\int_\Omega(\alpha\nabla.\boldsymbol{u})q^*\,\mathrm{d}\Omega - i\int_\Omega\frac{1}{M}p\,q^*\,\mathrm{d}\Omega+\frac{1}{\omega}\int_\Omega\nabla\cdot\left(\frac{\kappa}{\eta}\nabla p\right)q^*\,\mathrm{d}\Omega = 0.\end{aligned} \tag{B9}$$

We then apply the divergence theorem to eq. (B9). We also use the constitutive eq. (B2) and the BC of eqs (B4) and (B5). However, we do not yet include the BC pertaining to the oscillatory test. Finally, we express the weak formulation of Biot's equation as: find $\boldsymbol{u}$ and p such that

$$\begin{aligned}&a\langle\boldsymbol{u},\boldsymbol{v}\rangle - b\langle\boldsymbol{v}^*,p^*\rangle = 0,\\ &-i\,b\langle\boldsymbol{u},q\rangle - d\langle p,q\rangle = 0,\end{aligned} \tag{B10}$$

where

$$\begin{aligned}a\langle\boldsymbol{u},\boldsymbol{v}\rangle &= \int_\Omega(2\mu\,\boldsymbol{\varepsilon}(\boldsymbol{u}):\boldsymbol{\varepsilon}(\boldsymbol{v}^*)+\lambda_d\nabla\cdot\boldsymbol{u}\,\nabla\cdot\boldsymbol{v}^*)\,\mathrm{d}\Omega,\\ b\langle\boldsymbol{u},q\rangle &= \int_\Omega\alpha\nabla\cdot\boldsymbol{u}\,q^*\,\mathrm{d}\Omega,\\ d\langle p,q\rangle &= i\int_\Omega\frac{1}{M}p\,q^*\,\mathrm{d}\Omega+\int_\Omega\frac{\kappa}{\eta}\nabla p\cdot\nabla q^*\,\mathrm{d}\Omega.\end{aligned} \tag{B11}$$

To include oscillatory tests, we express the displacement as $\boldsymbol{u} = \boldsymbol{u_o} + \boldsymbol{\Delta u}$. Using this expression, eq. (B10) becomes

$$\begin{aligned}&a\langle\boldsymbol{u_o},\boldsymbol{v}\rangle - b\langle\boldsymbol{v}^*,p^*\rangle = -a\langle\boldsymbol{\Delta u},\boldsymbol{v}\rangle,\\ &-i\,b\langle\boldsymbol{u_o},q\rangle - d\langle p,q\rangle = i\,b\langle\boldsymbol{\Delta u},q\rangle,\end{aligned} \tag{B12}$$

To find the finite element approximation of eq. (B12), we use a mesh τ, which discretizes the domain Ω. We also consider the approximated solutions $\boldsymbol{u^h} = \boldsymbol{u_o^h} + \boldsymbol{\Delta u}$ and p^h, and we let the test functions $\boldsymbol{v}$ and q be the interpolating basis functions $\boldsymbol{\Phi}$ and ϕ, respectively, defined in the mesh τ. We then express the solutions $\boldsymbol{u_o^h}$ and p^h as a linear combination of the basis functions $\boldsymbol{\Phi}$ and ϕ, respectively. Finally, eq. (B12) reduces to the following linear system

$$\begin{vmatrix}\boldsymbol{A} & -\boldsymbol{B}^T\\ -i\,\boldsymbol{B} & -D\end{vmatrix}\begin{vmatrix}\boldsymbol{U}\\ \boldsymbol{P}\end{vmatrix} = \begin{vmatrix}\boldsymbol{f}\\ \boldsymbol{g}\end{vmatrix}, \tag{B13}$$

where the $\boldsymbol{U}$ and $\boldsymbol{P}$ are the vectors associated with the unknown coefficients of the discrete solutions of displacement $\boldsymbol{u_o^h}$ and pressure p^h defined at every node of the mesh. $\boldsymbol{A}$, $\boldsymbol{B}$ and $\boldsymbol{D}$ are the matrices associated with the bilinear forms a, b and d, respectively, where $A_{ij} = a\langle\Phi_j,\phi_i\rangle$, $B_{kj} = b\langle\Phi_j,\phi_k\rangle$ and $D_{kl} = a\langle\phi_l,\phi_k\rangle$. The components of the right-hand side vectors f and g are defined as $f_j = -a\langle\Delta u,\Phi_j\rangle$ and $g_k = i\,b\langle\Delta u,\phi_k\rangle$, respectively.

APPENDIX C: PP REFLECTION COEFFICIENT OF A VISCOELASTIC FRACTURE EMBEDDED IN ELASTIC HALF-SPACES

We consider a model as shown in Fig. 3, which consists of an infinite horizontal fracture represented by a thin viscoelastic layer Ω_v embedded in the elastic half-spaces Λ_1 and Λ_2. We further assume that both elastic half-spaces have the same rock physical properties. We are interested in finding the PP reflection coefficient of a normally incident wave striking at the interface of the viscoelastic fracture with the upper half-space Λ_1. We describe in the following the procedure to find the aforementioned PP reflectivity, which entails defining the governing equations, proposing the plane-wave solutions and setting the appropriate continuity equations to find the wave amplitudes.

We formulate the elastic and viscoelastic wave equations in the space-frequency domain. For the elastic case, we define the displacement vector $\boldsymbol{u}^e = \boldsymbol{u}^e(\boldsymbol{x},\omega)$ for any position $\boldsymbol{x}\in n$, with $n = \{\Lambda_1,\Lambda_2\}$ and angular frequency $\omega\in F$, with $F = (0, W]$. We also introduce the stress tensor field $\boldsymbol{\sigma}^e$ acting upon the medium. We then express the corresponding equation of motion as

$$-\rho_b\,\omega^2\,\boldsymbol{u}^e = \nabla.\boldsymbol{\sigma}^e \quad \text{in} \quad n\times F. \tag{C1}$$

The associated constitutive equation is given by

$$\boldsymbol{\sigma}^e = \mu\,\left(\nabla\boldsymbol{u}^e + (\nabla\boldsymbol{u}^e)^T\right) + \lambda\,\nabla.\boldsymbol{u}^e\;\boldsymbol{I}, \tag{C2}$$

where λ is the undrained Lamé modulus and is defined as $\lambda = \lambda_d + M\alpha^2$.

For the viscoelastic case, we define the corresponding displacement vector $\boldsymbol{u}^v = \boldsymbol{u}^v(\boldsymbol{x},\omega)$ for any position $\boldsymbol{x}\in\Omega_v$ and angular frequency $\omega\in F$, with $F = (0, W]$. Additionally, we define $\boldsymbol{\sigma}^v$ as the stress tensor acting upon the medium. The expressions for the corresponding equation of motion and constitutive equation remain identical to eqs (C1) and (C2), respectively. However, for the viscoelastic version the undrained Lamé modulus is frequency-dependent. This is $\lambda = \lambda(\omega) = H(\omega) - 2\mu$.

As previously stated, we consider an incoming P wave that impinges normally onto the interface Π_1 between the upper half-space and the fracture (Fig. 3). Since the half-spaces and the fracture are represented by elastic and viscoelastic media, respectively, only P waves propagate vertically in these media. Then, to find the total displacement in each medium, we sum the corresponding contributions of upgoing and downgoing P waves. We propose plane-wave solutions for the displacements in the elastic half-spaces and in the viscoelastic thin layer, respectively.

For the elastic half-spaces $n = \{\Lambda_2,\Lambda_2\}$, we calculate the total displacements u_N^e as

$$\begin{aligned}&u_N^e = u_{n\,D_P}^e + u_{n\,U_P}^e \quad \text{when}\, n = \Lambda_1,\ \text{or}\\ &u_N^e = u_{n\,D_P}^e \quad \text{when}\, n = \Lambda_2,\end{aligned} \tag{C3}$$

where D_P and U_P refer to the downgoing and upgoing P waves, respectively. In the first line of eq. (C3), the first and second terms on the right-hand side represent the contributions of the incident and reflected waves in the upper half-space Λ_1, respectively. Likewise,

in the second line of the same equation, the right-hand side term denotes the contribution of the transmitted wave in the lower half-space Λ_2.

Then, we express the corresponding displacements $u^e_{n\,j}$ with $n = \Lambda_1$ and Λ_2, and $j = D_P$ or U_P, as

$$u^e_{n\,j} = E_{n\,j}\ \exp[\pm\, i\ k^e_n\ x_3]\,, \tag{C4}$$

where $E_{n\,j}$ is the amplitude of the corresponding displacement and x_3 is the position. Negative and positive signs in the exponential correspond to downgoing and upgoing waves, respectively, k^e_n is the elastic scalar wavenumber for the P wave in medium n, calculated as $k^e_n = \omega/\,V^n_P$, where V^n_P is the P-wave velocity of medium n, with $V^n_P = \sqrt{(\lambda^n + 2\,\mu^n)/\rho^n_b}$, where $\rho^n_b = \phi^n \rho^n_{\rm f} + (1-\phi^n)\rho^n_{\rm s}$ is the bulk density of medium n.

For the viscoelastic medium Ω_v, we calculate the total displacement u^v as

$$u^v = u^v_{D_P} + u^v_{U_P}. \tag{C5}$$

Then, we express the solution of the displacement u^v_j, with $j = D_P, U_P$ as

$$u^v_j = V_j\ \exp[\pm\, i\ k^v\ x_3]\,, \tag{C6}$$

where V_j is the displacement amplitude, k^v is the viscoelastic scalar wavenumber for the P wave calculated as $k^v = \omega/\,V_P(\omega)$, where $V_P(\omega)$ is the complex-valued and frequency-dependent P-wave velocity that is computed as $V_P(\omega) = \sqrt{H(\omega)/\rho^v_b}$, where $\rho^v_{\rm b} = \phi^v \rho^v_{\rm f} + (1-\phi^v)\rho^v_{\rm s}$ is the bulk density of viscoelastic medium Ω_v.

If we assume that the amplitude of the incident P wave is one, then the reflection coefficient R_{PP} at the upper half-space is equal to $E_{\Lambda_1\,U_P}$ (eq. C4). To solve for the unknown amplitudes, we assemble a system of equations by imposing continuity of both displacements and tractions across the interfaces Π_q, with $q = 1, 2$, which separate the elastic and viscoelastic media, respectively (Fig. 3).

$$\begin{aligned} \left(u^e_{\rm N} - u^v\right)\big|_{\Pi_q} &= 0\,, \\ \left(t^e_{\rm N} - t^v\right)\big|_{\Pi_q} &= 0\,. \end{aligned} \tag{C7}$$

Here, $n = \Lambda_q$, $t^e_{\rm N} = (\boldsymbol{\sigma_{\rm N}}^e \cdot \hat{\boldsymbol{x}}_{\boldsymbol{3}}) \cdot \hat{\boldsymbol{x}}_{\boldsymbol{3}}$ and $t^v = (\boldsymbol{\sigma}^v \cdot \hat{\boldsymbol{x}}_{\boldsymbol{3}}) \cdot \hat{\boldsymbol{x}}_{\boldsymbol{3}}$ are the normal traction components on the elastic and viscoelastic sides of the interface, respectively.